Nano Research
2021, 14(3): 555–569

ISSN 1998-0124 CN 11-5974/O4
https://doi.org/10.1007/s12274-020-3049-5

Review Article

Iron-group electrocatalysts for ambient nitrogen reduction reaction in aqueous media

Benyuan Ma[1,2], Haitao Zhao[1], Tingshuai Li[1], Qian Liu[1], Yongsong Luo[1], Chengbo Li[1], Siyu Lu[3], Abdullah M. Asiri[4], Dongwei Ma[5] (✉), and Xuping Sun[1] (✉)

[1] *Institute of Fundamental and Frontier Sciences, University of Electronic Science and Technology of China, Chengdu 610054, China*
[2] *College of Physics and Electronic Engineering, Nanyang Normal University, Nanyang 473061, China*
[3] *Green Catalysis Center and College of Chemistry, Zhengzhou University, Zhengzhou 450001, China*
[4] *Chemistry Department, Faculty of Science & Center of Excellence for Advanced Materials Research, King Abdulaziz University, P.O. Box 80203, Jeddah 21589, Saudi Arabia*
[5] *Key Laboratory for Special Functional Materials of Ministry of Education, and School of Materials Science and Engineering, Henan University, Kaifeng 475004, China*

Received: 29 June 2020 / **Revised:** 2 August 2020 / **Accepted:** 10 August 2020

ABSTRACT

Electrochemical nitrogen reduction reaction (NRR) is considered as an alternative to the industrial Haber-Bosch process for NH_3 production due to both low energy consumption and environment friendliness. However, the major problem of electrochemical NRR is the unsatisfied efficiency and selectivity of electrocatalyst. As one group of the cheapest and most abundant transition metals, iron-group (Fe, Co, Ni and Cu) electrocatalysts show promising potential on cost and performance advantages as ideal substitute for traditional noble-metal catalysts. In this minireview, we summarize recent advances of iron-group-based materials (including their oxides, hydroxides, nitrides, sulfides and phosphides, etc.) as non-noble metal electrocatalysts towards ambient N_2-to-NH_3 conversion in aqueous media. Strategies to boost NRR performances and perspectives for future developments are discussed to provide guidance for the field of NRR studies.

KEYWORDS

nitrogen reduction reaction, electrochemical NH_3 synthesis, iron-group catalysts, ambient conditions

1 Introduction

NH_3 is an important chemical material that is widely used in industrial and agricultural production, such as aqueous ammonia, dye, plastic, explosive and fertilizer, etc. [1]. The annual global ammonia production has exceeded 200 million tons, and 80% of which is used to the synthesis of fertilizer, which contributes important part to the rapid economic development and population growth [2]. NH_3 is also considered as an attractive hydrogen carrier (17.6 wt.%), due to the advantages of high energy density (4.3 $kWh{\cdot}kg^{-1}$), carbon-free nature and easy transport (−33 °C, liquid) [3]. In traditional industry, NH_3 is produced from N_2 and H_2 feeding gases via the Haber-Bosch process, which requires high pressure (150–350 atm), temperature (350–550 °C) and Fe-based catalysts [4]. However, industrial H_2 is mainly produced by the high-temperature reactions between H_2O and carbon-containing compounds, e.g., C, CO, CH_4, CH_3OH, and the Haber-Bosch process using this H_2 source suffers from heavy energy consumption and serious CO_2 emission, contributing to 2% of global energy consumption and 1% of greenhouse gas. Inspired by the biological N_2 fixation of nitrogenase [5, 6], ambient NH_3 synthesis becomes an economic and environment-friendly strategy. Electrocatalytic nitrogen reduction reaction (NRR), which can synthesize NH_3 from N_2 and water at ambient conditions without releasing greenhouse gas, becomes a promising alternative to the Haber-Bosch process but needs efficient electrocatalysts to drive the NRR [7–9].

Generally, noble-metal catalysts show remarkable performances, but the high cost and scarcity limit their large-scale applications [10–13]. Therefore, research focus has been shifted to noble-metal-free alternatives [14–29]. Typically, transition metal (TM)-based materials are promising NRR catalysts due to the abundant d-orbital electrons and unoccupied orbitals for the activation of strong N≡N triple bond [30, 31]. Among them, iron-group (Fe, Co, Ni and Cu) [32] electrocatalysts are considered to be ideal substitute for noble-metal catalysts. Moreover, iron-group elements are of active metals easy to be compounded with other elements, such as modifying into oxides, hydroxides, nitrides, sulfides and phosphides, which may possess unusual and remarkable catalytic activation and stability.

Here, we summarize the recent advances of iron-group catalysts for electrochemical NRR under ambient conditions in aqueous media. Firstly, we analyze the NRR mechanisms and discuss the strategies to boost the NRR performances. Then, we present the fabrication and application achievements of Fe–, Co–, Ni–, Cu– and multi-iron-based catalysts, including their oxides, hydroxides, nitrides, sulfides and phosphides, even metal organic frameworks (MOFs), as noble-metal-free electrocatalysts

Address correspondence to Xunping Sun, xpsun@uestc.edu.cn; Dongwei Ma, dwmachina@126.com

for N_2-to-NH_3 conversion. Finally, we outlook the future perspectives and provide some insights into the development of electrochemical NRR.

2 Fundamental mechanisms of NRR

N atom has five valence electrons with an electronic configuration of $2s^22p^3$, which means three unoccupied 2p orbitals and hence the high reactive activity of single N atom. However, the very stable N_2 molecule can be easily formed by the linear combination of atomic orbitals between two N atoms. As shown in Fig. 1(a), the hybrid orbitals consists of four bonding orbitals (two σ and two π) and four antibonding orbitals (two σ* and two π*), in which two σ, one σ* and two π orbitals are fully occupied by the coupled spin electrons while other orbitals display empty state [2, 33]. It is well known that the σ or σ* chemical bonds usually present very high bonding energy such as that the highly inert diamond has four this type of bonds [34]. For N_2, the three occupied σ and σ* orbital bonds also contribute to its inert properties. It needs a high energy input of 945 kJ·mol^{-1} to directly cleave the N≡N triple bond, which can well explain why the harsh conditions of Haber-Bosch process [2, 35]. In addition, there is a large band gap (10.82 eV) between the lowest unoccupied molecular orbital (LUMO) and the highest occupied molecular orbital (HOMO) and a high ionization energy (15.58 eV), which certainly prevent the electron transfer [2, 33]. As shown in Fig. 1(c), the basic mechanisms for N_2-to-NH_3 conversion can be classified into two types, including dissociative and associative pathways [30, 35–37]. The dissociative pathway mainly concerns with the Haber-Bosch process, where the high energy input firstly cleave the N≡N triple bond to obtain isolated N atoms which then react with H atoms to form NH_3 molecules. As to associative pathway, hydrogenation process occurs but keeping the two N atoms of N_2 bond with each other before the first NH_3 is generated. According to the bonding pattern between N_2 and active sites, the associative pathway can be further divided into end-on and side-on patterns. For the end-on pattern, only one N atom of N_2 is bonded to active sites while in side-on pattern is the both N atoms bonded to active sites [30, 35]. Further, according to the hydrogenation order, the end-on pattern has two ways for producing NH_3, namely distal and alternating pathways, while the side-on one only has enzymatic pathway. In the distal pathway, proton-electron pairs firstly attack the N atom away from the active N_2 is reduced to NH_3. As can be seen, the key step is to promote the electron exchange between N_2 and catalyst. Namely, after N_2 adsorption on catalyst surface, the N_2 donates the electrons from its bonding orbitals, and at the same sites to generate one NH_3, and then attack the other N atom of N_2. In the alternating pathway, the proton-electron pairs attack the two N atoms alternatively, with the second NH_3 released just after the first NH_3. The enzymatic pathway has a similar hydrogenation process with the alternating pathway [30, 35]. In addition, for the end-on pattern, the hydrogenation may proceed through a so-called hybrid pathway, where at the third hydrogenation step the distal pathway may switch to the alternating one, depending on the relative free energy change (as denoted by the dotted arrow in Fig. 1(c)).

In fact, the associative pathway initially is inspired by the biological nitrogenase (Fig. 1(b)). Typically, in the N_2 fixation process of FeMo-dependent enzyme, the electrons are provided by the hydrolysis of 16 adenosine 5'-triphosphate (ATP), then the electrons are transferred by Fe-protein to the metal cluster FeMo cofactor, where time, accepts the injected foreign electrons into its antibonding π* orbital, which activate the N_2 and offer a mild kinetic way for further hydrogenation to form NH_3 [2, 38, 39]. For the electrochemical NRR, the ATP-hydrolysis electrons are replaced by the electrons driven from external electrode. No matter which way, N_2 adsorption, activation, hydrogenation and NH_3 desorption are the essential steps. For the electrochemical NRR, a typical way to promote N_2 adsorption is selecting appropriate catalyst to provide beneficial active sites. Besides of the biological FeMo cofactor [36, 39], some other transition metals also have this ability to adsorb and activate N_2 by using

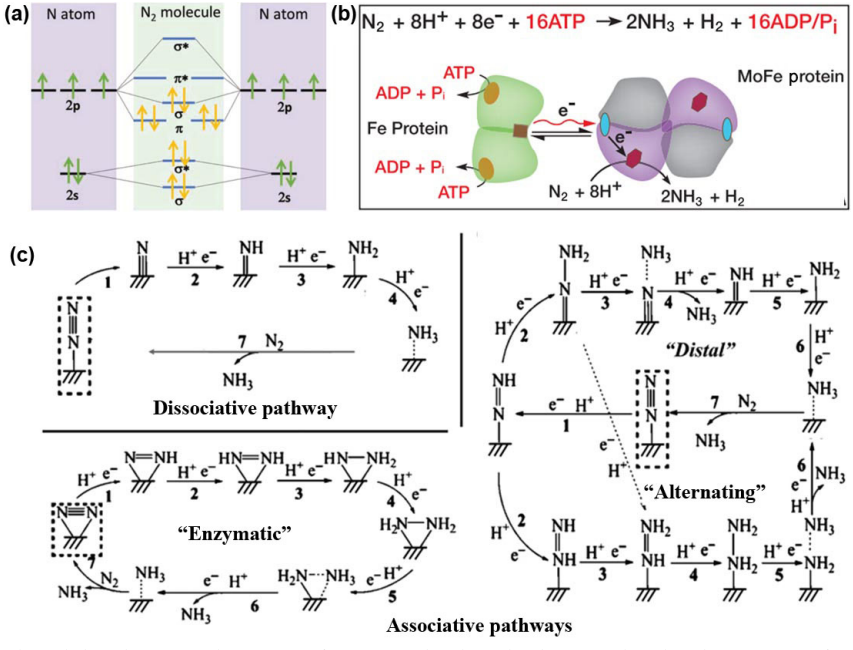

Figure 1 (a) N atom orbitals and their linear combination to form N_2 molecular orbitals. Reproduced with permission from Ref. [2], © WILEY-VCH Verlag GmbH & Co. KGaA, Weinheim 2018. (b) N_2 reduction reaction catalyzed by nitrogenase Fe protein and MoFe protein. Reproduced with permission from Ref. [38], © American Association for the Advancement of Science 2016. (c) Schematic of reaction pathways for the N_2-to-NH_3 conversion, including the dissociative and associative pathways (distal, alternative, enzymatic and hybrid pathways). Reproduced with permission from Ref. [36], © American Chemical Society 2016. Reproduced with permission from Ref. [37], © WILEY-VCH Verlag GmbH & Co. KGaA, Weinheim 2018.

their abundant d-orbital electrons, empty or unoccupied orbitals to drive the famous donation-acceptance process with N_2 [40–43]. Besides of this, the redistribution of charge density of catalyst is also a feasible way to promote the N_2 adsorption, such as by vacancy engineering [44–46], edge adsorption [47], heterojunction [48] and heteroatoms doping [49–52]. Of course, the catalyst with high specific surface area is another way to enhance the N_2 adsorption because it can provide more exposed active sites [53–56]. Finally, the N_2 concentration in the reaction solvent should be considered because the animate gas-liquid-solid interface exchange can raise the N_2 adsorption rate [57]. The N_2 activation usually occurs in the donation-acceptance process. However, in most cases the direct N_2 activation by catalyst is underpowered, e.g., without obvious bond length or bonding energy changes of N≡N. Hence, for sufficient activation, it is necessary to use a negative electrode potential to excite electrons injecting into the antibonding π^* orbital of N_2 [2]. Of course, there are other electron injecting method, such as photo-induced electrons and plasmon-driven hot electrons [58–60]. At this vital activation step, a free energy uphill usually occurs concerning the formation of $*N_2$ or $*N_2H$ [35, 43, 61]. During the hydrogenation process, the catalytic environment can influence the different hydrogenation orders and pathways, resulting in different products such as NH_3, N_2H_4 and H_2 [2]. As to NH_3 desorption, the density functional theory (DFT) calculations reveal that the destabilizing of $*NH_2$, especially on strong-binding active site, is usually crucial because it is beneficial to reduce the free energy uphill during the formation of $*NH_3$ and the final desorption energy [35, 43, 61]. In fact, the produced NH_3 can be easily dissolved into water, which effectively promotes the release of the active sites for the next catalytic cycle. Finally, electrons exchange occurs in the overall NRR process, hence a conductive catalyst substrate is very necessary to facilitate the injection of enough electrons to the active sites to support continuous N_2 reduction reaction [2, 62, 63].

To satisfy the practical application, another urgent problem is to overcome the low NH_3 yield and Faraday efficiency (FE), which mainly originate from the following reasons. Firstly, there is nearly an overlap between the standard equilibrium potential of electrocatalytic NRR (0.092 V vs. reversible hydrogen electrode (RHE)) and that of the hydrogen evolution reaction (HER, 0 V vs. RHE) [33, 64]. Hence, the competitive HER side reaction consumes most of the reactive electrons. Secondly, the N-related intermediates with high free energy barriers during hydrogenation or NH_3 desorption may impede the active sites and then facilitate the HER [43, 61]. Finally, the catalyst features, such as intrinsic catalytic activity, porosity, specific surface area and substrate conductivity, also can influence the NH_3 production efficiency [65].

3 Iron-group NRR electrocatalysts

3.1 Fe-based electrocatalysts

Fe is not only the component element of the known nitrogenase (Fe-protein and MoFe-protein) for biological N_2 fixation but also widely utilized in the Haber-Bosch process for industrial NH_3 synthesis [4, 38]. Transition metal oxides, nitrides, carbides and sulfides are common catalysts for NRR. Among them, the metal oxides have gathered the most attention owing to easy synthesis on a large scale, tunable activity, considerable stability and relative environment benignity [66]. In a theoretical study by Nguyen et al. [67], DFT calculations were carried out to investigate the catalytic action of Fe_2O_3. It suggests that N_2 can be adsorbed on the Fe_2O_3 (0001) surface by following an associative mechanism. The Fe ion adsorbs and activates the N_2 molecule, with the first hydrogenation as the potential-limiting step needing an energy barrier of 1.14 eV. Kong et al. [68] reported that, in 0.1 M KOH electrolyte, the γ-Fe_2O_3 nanoparticles cam catalyze the N_2-to-NH_3 conversion at low temperatures (≤ 65 °C), attaining a NH_3 yield of 12.5 $nmol \cdot h^{-1} \cdot mg^{-1}_{cat}$ and a FE of 1.9%.

To further improve NH_3 yield and FE, it is an effective method to introduce defects in catalyst to redistribute charge density and induce active sites. In Figs. 2(a)–2(d), as the surface oxygen vacancies (OVs) of Fe_2O_3 are enriched by annealing in Ar, the catalyst loaded on carbon nanotubes (o-Fe_2O_3-Ar/CNT) presents greatly improved NH_3 yield and FE in 0.1 M KOH with the values of 0.46 $\mu g \cdot h^{-1} \cdot cm^{-2}$ and 6.04% at −0.9 V, respectively [45]. Catalyst substrate with high electrical conductivity is also essential for NRR, because the abundant electrons in substrate can increase the possibility of electron injection into the antibonding orbital of N_2 and also facilitate the following nitrogen reduction [69]. In Chen's study, the beneficial role of catalyst substrate was investigated. As the Fe_2O_3 supported on carbon nanotubes is used as catalyst (Fe_2O_3-CNT), a higher NH_3 yield of 2.2×10^{-3} $g \cdot m^{-2} \cdot h^{-1}$ is obtained versus the 1.0×10^{-3} $g \cdot m^{-2} \cdot h^{-1}$ of Fe_2O_3 [70]. Besides of this, the NRR stability must be considered because the Fe_2O_3 electrocatalyst will be etched in acid electrolyte or reducd into $Fe^{(I)}/Fe^{(II)}$ in alkaline electrolyte [45, 68, 70]. Based on this, the NRR performances of Fe_2O_3 nanorods and Fe_2O_3-rGO have been investigated in neutral conditions such as 0.1 M Na_2SO_4 and 0.5 M $LiClO_4$, attaining higher NH_3 yields of 15.9 and 22.13 $\mu g \cdot h^{-1} \cdot mg^{-1}_{cat}$,

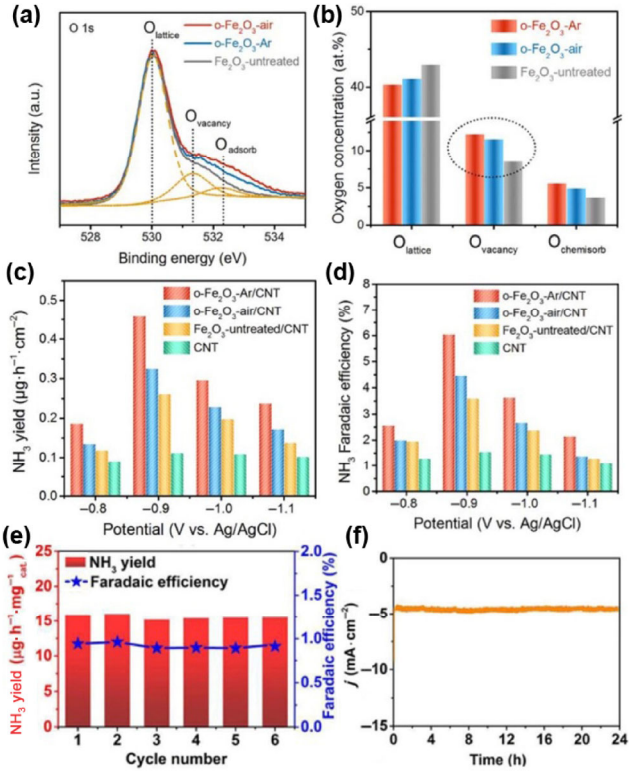

Figure 2 (a) O 1s X-ray photoelectron spectroscopy (XPS) spectra of o-Fe_2O_3-Ar, o-Fe_2O_3-air and Fe_2O_3-untreated, where the dash lines show the location of three individual peaks. (b) Concentrations comparison of the three different oxygen species obtained from the O 1s XPS spectra. (c) Average NH_3 formation rate and (d) FEs of the different catalysts. Reproduced with permission from Ref. [45], © Wiley-VCH Verlag GmbH & Co. KGaA, Weinheim 2018. (e) NH_3 yields and FEs of the Fe_2O_3 nanorods catalyst at −0.8 V during recycling tests. (f) Time-dependent current density curve for Fe_2O_3 nanorods catalyst at the potential of −0.8 V. Reproduced with permission from Ref. [71], © Wiley-VCH Verlag GmbH & Co. KGaA, Weinheim 2018.

respectively [71, 72]. As confirmed in Figs. 2(e) and 2(f), Fe_2O_3 nanorods display good cycling stability and long-term durability in neutral electrochemical environment.

Our recent work suggests that β-FeOOH nanorods perform efficiently for NRR electrocatalysis [73]. DFT calculations reveal that Fe active sites play a key role in activating N_2 molecules. In 0.5 M $LiClO_4$, β-FeOOH nanorods (Fig. 3(a)) achieve a high NH_3 yield of 23.32 $\mu g \cdot h^{-1} \cdot mg^{-1}_{cat.}$ with a FE of 6.7% (Fig. 3(b)). In addition, the favorable role of Li^+ in enhancing NRR performances was also studied by using different electrolytes such as $LiClO_4$, $NaClO_4$ and $KClO_4$. The NH_3 yields and FEs drop with the cation size order of $Li^+ < Na^+ < K^+$, which is ascribed to the relatively strong interaction between counterions and N_2. The Li^+ counterion layer may restrict the approach of H_2O molecules to the reactive sites and hence suppress the competitive HER [73, 74]. It further suggests the NRR activity of β-FeOOH nanorods can be greatly enhanced by F doping which was realized by adding NaF at the hydrothermal step [75]. F has an electronegativity of 3.98 larger than that of O (3.44) and Fe (1.83). F doping leads to significant charge redistribution and positively charged Fe active site. This Lewis acid site is beneficial to adsorbing N_2 which is of weak Lewis base [33]. As a result, β-FeO(OH,F) nanorods (Fig. 3(c)) obtain a NH_3 yield of 42.38 $\mu g \cdot h^{-1} \cdot mg^{-1}_{cat.}$ and FE of 9.02% (Fig. 3(d)), outperforming pristine β-FeOOH (10.01 $\mu g \cdot h^{-1} \cdot mg^{-1}_{cat.}$, 2.16%). Besides, F doping leads to a decrease in NRR overpotential for highest NH_3 yield from −0.75 down to −0.6 V. DFT results reveal that the next-nearest Fe atom from the F atom is the favorable active site for N_2 adsorption and reduction. The N≡N is better activated as the bond length is elongated to 1.163 Å versus 1.146 Å for pristine β-FeOOH. Charge density

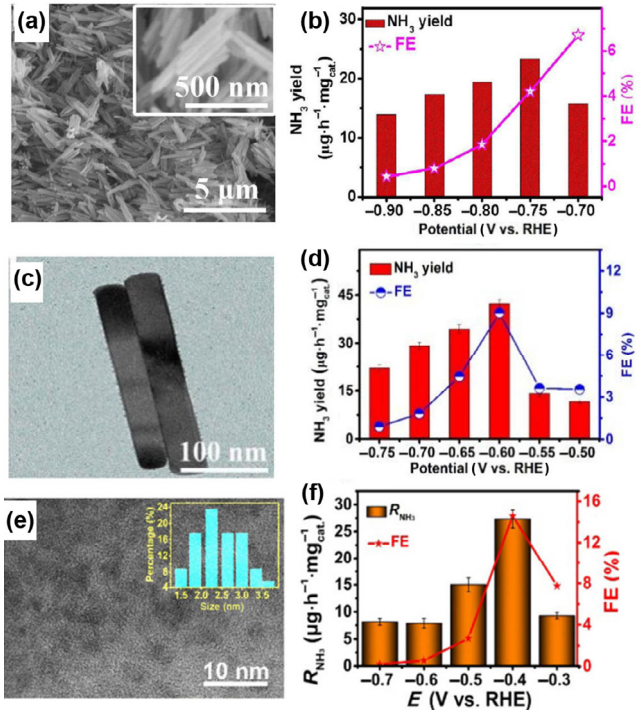

Figure 3 (a) Scanning electron microscopy (SEM) images and (b) corresponding NH_3 yields and FEs of β-FeOOH. Reproduced with permission from Ref. [73], © The Royal Society of Chemistry 2018. (c) Transmission electron microscopy (TEM) image and (d) corresponding NH_3 yields and FEs of β-FeO(OH,F). Reproduced with permission from Ref. [75], © This journal is © The Royal Society of Chemistry 2019. (e) High resolution TEM (HRTEM) image and (f) corresponding NH_3 yields and FEs of FeOOH QDs-GS. Reproduced with permission from Ref. [76], © Tsinghua University Press and Springer-Verlag GmbH Germany, part of Springer Nature 2019.

difference suggests enhanced charge exchange between Fe active site and N_2 for β-FeO(OH,F). However, FeOOH suffers from intrinsic low electrical conductivity. To solve this issue, we developed FeOOH quantum dots decorated graphene sheet (FeOOH QDs-GS, Fig. 3(e)) toward enhanced NRR performances [76]. These nanocatalysts loaded on the graphene are able to not only prevent the nanocatalyst aggregation from stacking (1.3–1.5 nm) but improve the overall catalytic performance owing to more exposed active sites and lower charge transfer resistance. As shown in Fig. 3(f), the FE (14.6%) of the catalyst is significantly improved.

Fe atom has an electronic configuration of $4s^2 3d^6$, which means four unpaired d spin electrons. Fe^{2+} has two empty and two half-occupied orbitals, while Fe^{3+} has three empty but a half-occupied orbitals. These electronic configurations are very beneficial to drive the acceptance-donation process with the adsorbed N_2. Hence, except for the mainly focused Fe_2O_3 and FeOOH catalysts, Fe-based catalysts with low valence states (e.g., Fe and Fe_3O_4) are necessary to be investigated. We *in situ* synthesized Fe_3O_4 nanorods on Ti mesh (Ti/Fe_3O_4) for N_2 reduction electrocatalysis, attaining a NH_3 yield of 5.6×10^{-11} $mol \cdot s^{-1} \cdot cm^{-2}$ and a FE of 2.6% in 0.1 M Na_2SO_4 [77]. Furthermore, the Fe^{3+} of Fe_2O_3 may be reduced under electrochemical environment and the low-valence iron ions may have surprising activity for NRR [78]. In Hu's study [79], a NRR catalyst was *in situ* synthesized by the electrochemical reduction of Fe/Fe_2O_3 into Fe/Fe_3O_4. The obtained Fe/Fe_3O_4 possesses a porous surface morphology and favorable conductivity versus Fe_2O_3 or Fe_3O_4. As a result, the Fe/Fe_3O_4 catalyst displays enhanced NRR activity and effective suppression to HER, attaining a high FE of 8.29% which is about 120 times higher than that of bare Fe foil, also superior to that of Fe_3O_4 and Fe_2O_3 nanoparticles. In addition, Fe can serve as an effective dopant to enhance the NRR performances of TiO_2 and the resulting Fe-TiO_2 attains a superior FE of 25.6 % and a NH_3 yield of 25.47 $\mu g \cdot h^{-1} \cdot mg^{-1}_{cat.}$ in 0.5 M $LiClO_4$ [80]. DFT calculations indicate that introducing Fe into TiO_2 (101) increases the number of OV, thereby further promoting N_2 activation. The synergistic effect of bi-Ti_3^+ and OVs contributes to the high NRR performances. The favorable role of OVs is also adopted in Fe-based pervskite for NRR. In Zhang's work [81], OVs were introduced into $LaFeO_3$ perovskite by doping Cs and Ni. The catalyst displays enhanced catalytic activity for NRR, attaining a NH_3 yield of 13.46 $\mu g \cdot h^{-1} \cdot mg^{-1}_{cat.}$ and a FE of 1.99% under alkaline condition. We developed porous $LaFeO_3$ nanofiber with abundant active sites and OVs by using electrospinning technique and 600 °C H_2/Ar annealing. When tested in 0.1 M HCl, 18.59 $\mu g \cdot h^{-1} \cdot mg^{-1}_{cat.}$ NH_3 yield and 8.77% FE are obtained [82]. DFT calculations indicate that the exposed metallic ions with newly localized electronic states near the Fermi level facilitate both the N_2 activation and the subsequent hydrogenation via enzymatic pathway.

The nitrogenous carbon framework anchored with metal atoms is also promising material for NRR under ambient conditions. DFT calculations predicate that FeN_3-embedded graphene is a promising NRR catalyst, in which the FeN_3 centers with high-spin polarization are considered as effective active sites [37]. Wang et al. [83] designed a Fe-N/C-CNTs electrocatalyst (Fig. 4(a)) by carbonizing Fe-doped zeolitic-imidazolate framework (ZIF) deposited on the surface of carbon nanotubes (CNTs). The porous structure, large active surface area, positively charged surface, weak ferromagnetism and strong nitrogen chemisorption are favorable for the NRR electrocatalysis. The electrocatalyst exhibits a high NH_3 yield of 34.83$\mu g \cdot h^{-1} \cdot mg^{-1}_{cat.}$ and a FE of 9.28% at −0.2 V in 0.1 M KOH.Compared with

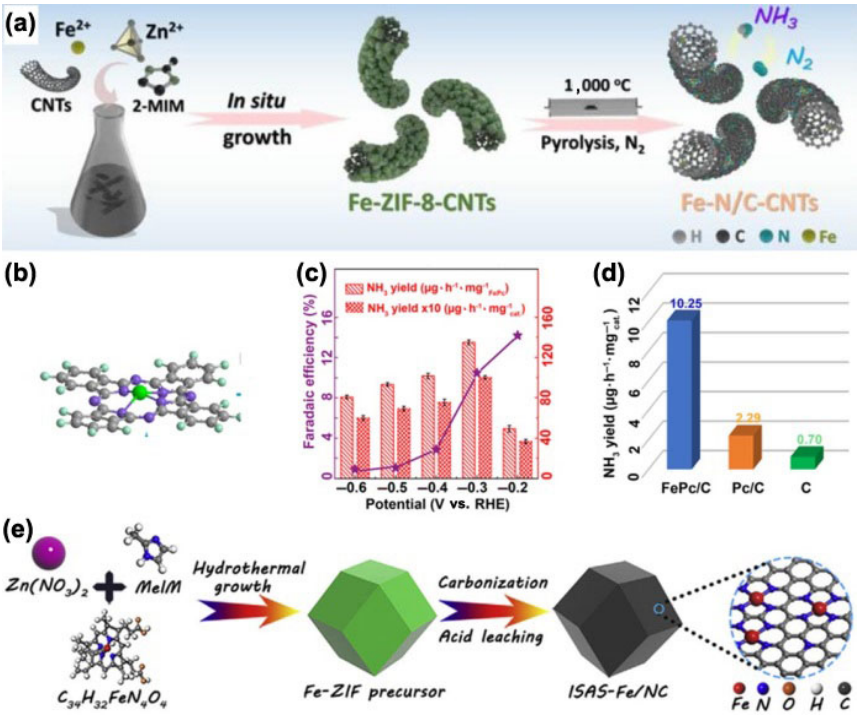

Figure 4 (a) Schematic of the synthesis of Fe-N/C-CNTs catalyst. Reproduced with permission from Ref. [83], © American Chemical Society 2019. (b) Geometric structure of FePc. (c) NH_3 yields and FEs of FePc/C. (d) Comparison of NH_3 yields and FEs of FePc/C, Pc/C and porous carbon. Reproduced with permission from Ref. [84], © American Chemical Society 2019. (e) Schematic of the synthesis of ISAS-Fe/NC catalyst. Reproduced with permission from Ref. [87], © Elsevier Ltd. 2019.

CNTs or N/C-CNTs, the introduction of Fe atoms into N/C-CNTs enhances the NRR performance. DFT calculations indicate that the built-in Fe-N_3 species plays a primary role for NH_3 synthesis. N_2 can be spontaneously adsorbed on the Fe-N_3 species with a free energy of −0.75 eV, and the central Fe site with significant spin moment is the active site. The Fe-N_3 and the around carbon atoms can interact and suppress HER. The N_2 reduction favors a distal pathway with the energy barrier of 0.84 eV from $*N_2$ to $*N_2H$. Similarly, He et al. synthesized a FePc/C electrocatalyst via 200 °C annealing the iron phthalocyanine (Pc) which was loaded on porous carbon [84]. The built-in Fe-N_4 species plays a crucial role for NH_3 synthesis, demonstrating a percussive NH_3 yield of 137.95 $\mu g \cdot h^{-1} \cdot mg^{-1}_{cat.}$ and a FE of 10.50% at −0.3 V in 0.1 M Na_2SO_4 (Figs. 4(b)–4(d)). By DFT calculations, the Fe central in Fe-N_4 is identified as the most active site for NRR, and the preferred route is the alternating pathway with an energy barrier of 0.85 eV at the first hydrogenation step. Metal organic framework (MOF) is another material to make Fe-N-C structures. Because of the porous structure and the high specific surface areas, MOF materials provide a large number of adsorption sites for N_2 molecules. In Zhao's work, a series of MOFs (M = Fe, Co and Cu) were hydrothermally prepared using 1,3,5-benzenetricarboxylic acid or 2-methylimidazole as ligand [85]. The uniformly distributed metal ions (Fe^{3+}, Co^{3+} and Cu^{2+}) own empty *d* orbitals, hence providing Lewis acid sites to accept electrons from N_2 and loosen N≡N bond. Among these catalysts, MOF(Fe) offers the highest NH_3 yield of 2.12×10^{-9} $mol \cdot s^{-1} \cdot cm^{-2}$ with a FE of 1.43%. Single-atom catalysts may also promsing as NRR catalysts with high catalytic efficiency and selectivity [61, 86]. In Lü's work [87], isolated single Fe atom sites were anchored on N-doped carbon framework (ISAS-Fe/NC) via carbonizing Fe-doped zeolitic imidazolate frameworks (ZIF-8) and then etching away Zn^{2+} (Fig. 4(e)). The formed Fe-N_3 species plays the key role of active sites. N_2 can be adsorbed on Fe atom by a favorable enzymatic pathway with energy barrier of 1.69 eV from *NN to *NNH. In 0.1 M PBS, the ISAS-Fe/NC exhibits a remarkable FE of 18.6% and a NH_3 yield of 62.9 $\mu g \cdot h^{-1} \cdot mg^{-1}_{cat.}$.

Last but not least to mention is the Fe-base sulfides and phosphides. In Zhao's work [88], Fe_3S_4 nanosheets with porous structure were prepared via solvothermal synthesis using polyethylene glycol 200 and thiourea as the deep eutectic solvent as shape-controlling agent and *in situ* sulfur source. The Fe_3S_4 nanosheets (Fig. 5(a)) drive an efficient and stable electrochemical N_2 reduction in 0.1 M HCl with a high NH_3 yield of 75.4 $\mu g \cdot h^{-1} \cdot mg^{-1}_{cat.}$ and FE of 6.45% at −0.4 V (Figs. 5(d) and 5(e)). Similar to the above mentioned Fe_3O_4, the low valence Fe^{2+} of FeS may also have excellent catalytic activity for NRR. By sulfurizing the surface of Fe foam, FeS/Fe (Fig. 5(b)) was obtained as a catalyst electrode for NRR, and it achieves a NH_3 yield of 4.13×10^{-10} $mol \cdot s^{-1} \cdot cm^{-2}$ and FE of 17.6% in 0.1 M KOH [89]. DFT calculations (Figs. 5(f) and 5(g)) indicate that, because of the well-suited Fe-Fe distance on the FeS(011) surface, the adsorbed dinitrogen changes from the end-on *NN configuration to the side-on *NNH* configuration at the first hydrogenation step, where the two N atoms are separately coordinated to two neighbor Fe atoms. The NRR prefers an alternating pathway with the first hydrogenation step as the potential-determining step (0.46 eV). Of note, phosphorous also has an unusual role in modulating the N_2 reduction activity of Fe-based catalyst. By controlling the amount of phosphorus during the phosphidation of Fe_2O_3-rGO, we successfully prepared FeP_2-rGO and FeP-rGO [90]. With increasing coordinated P to Fe atom, FeP_2-rGO catalyst (Fig. 5(c)) shows superior NRR performance to FeP-rGO because of the lower HER activity, the more negative N_2 adsorption energy and the more active sites. As shown in Fig. 5(h) and (i), FeP_2-rGO attains a larger NH_3 yield of 35.26$\mu g \cdot h^{-1} \cdot mg^{-1}_{cat.}$ and a higher FE of 21.99% in 0.5 M $LiClO_4$, outperforming FeP-rGO counterpart (17.13 $\mu g \cdot h^{-1} \cdot mg^{-1}_{cat.}$ NH_3 yield and 8.57% FE).

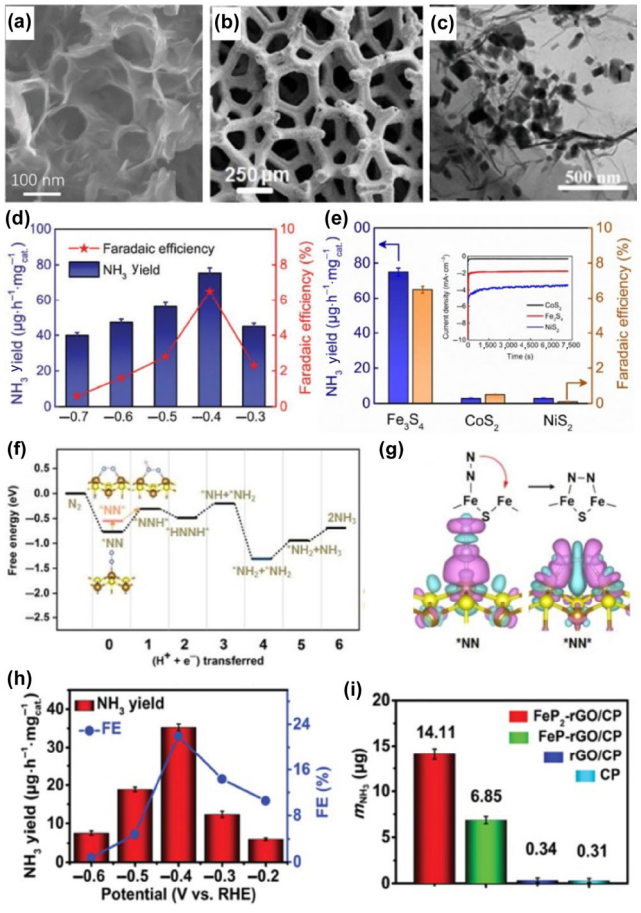

Figure 5 SEM images of (a) Fe_3S_4 and (b) FeS/Fe-foam. (c) TEM image of FeP_2-rGO. (d) NH_3 yields and FEs of Fe_3S_4. (e) Comparison NH_3 yields and FEs of Fe_3S_4, CoS_2 and NiS_2 catalysts at −0.4 V for 2 h. (f) Free energy diagram for the NRR on the FeS(011) surface. (g) Charge density difference of the N_2 adsorption on the FeS(011) surface. Red and green denote electron accumulation and depletion, respectively. (h) NH_3 yields and FEs of FeP_2-rGO. (i) NH_3 amount of FeP_2-rGO/CP, FeP-rGO/CP, rGO/CP, and bare CP at −0.40 V for 2 h. (a), (d), and (e) Reproduced with permission from Ref. [88], © The Royal Society of Chemistry 2018. (b), (f), and (g) Reproduced with permission from Ref. [89], © The Royal Society of Chemistry 2019. (c), (h), and (i) Reproduced with permission from Ref. [90], © The Royal Society of Chemistry 2019.

3.2 Co-based electrocatalysts

Co-based materials, e.g. CoO and Co_3O_4, have held great promise for energy applications in lithium battery [91], fuel cell [92], supercapacitor [93] and water splitting [94]. Co-based oxides were also be used to catalyze electrochemical NRR process. In Chu's work [66], by ultrafast combustion (few seconds) of GO/$Co(Ac)_2$ aerogel, the growth of CoO nanocrystals can be well restrained. Meanwhile, the combustion reduced the GO into the rGO by thermal deoxygenation (Fig. 6(a)). As a result, ultra-fine CoO quantum dots can be anchored on rGO substrate (CoO QD/rGO) (Fig. 6(b)). Benefited from the enhanced conductivity of rGO and the more exposed Co active sites, CoO QD/rGO exhibits a NH_3 yield of 21.5 $\mu g \cdot h^{-1} \cdot mg^{-1}_{cat.}$ and FE of 8.3% at −0.6 V in 0.1 M Na_2SO_4 for NRR (Fig. 6(c)). DFT calculations show that the dominating CoO(200) crystal surface has favorable N_2 adsorption capacity but poor HER activity. The CoO(200) crystal surface exhibits a perfect NRR selectivity with a negative $*N_2$ adsorption energy of −1.208 eV but positive *H adsorption free energy about 1.3 eV, which mean the preferential adsorption order of N_2 before the hydrogenation on $*N_2$. By using ZIF-67 MOF template, Luo et al. synthesized Co_3O_4@NCs with Co_3O_4 anchored on nitrogen-doped carbon structure [95]. The Co_3O_4@NCs has a core-shell inner structure (Fig. 6(d)). The electron spin resonance (ESR) spectra indicate a high concentration of OVs. It is believed that the OVs can trap the electrons in metastable state which may be injected into the antibonding orbital of N_2 to weaken the N≡N. The temperature programmed desorption (TPD) results confirm a favorable N_2 adsorption capacity. The core-shell structure also promotes the collision between the trapped N_2 and the catalytic surface. As a result, the catalyst shows an excellent NRR performance, achieving a NH_3 yield of 42.58 $\mu g \cdot h^{-1} \cdot mg^{-1}_{cat.}$ and a FE of 8.5% at −0.2 V in 0.05 M H_2SO_4 (Fig. 6(e)). Cobalt doping may be another effective way to boost NRR performances. In Zhang's work [96], Co-dopd MoS_{2-x} with S vacancies were directly grown on carbon cloth for N_2 fixation. Theoretical analysis on the NRR mechanism demonstrates that the Co doping can modify the powerful interaction between Mo and $*N_2$ from three bond number to one (Figs. 6(f) and 6(g)), hence cutting down the free energy barriers of N-related intermediates during NRR hydrogenation process. The required maximal free energy barrier decreases from 1.62 to 0.59 eV. The Co-doped MoS_{2-x} achieves a NH_3 yield over 0.6 $mmol \cdot h^{-1} \cdot g^{-1}$ and a FE over 10%, while the as-grown MoS_{2-x} only 0.32 $mmol \cdot h^{-1} \cdot g^{-1}$ and 1.7%.

Cobalt sulfides are also promising electrocatalysts for NRR because of the high electroconductivity and high catalytic activity [41, 97]. Chen et al. [98] constructed a Co-N/S-C bridging bond at the interface between CoS_2 nanoparticles and NS-G (nitrogen- and sulfur- doped reduced graphene), by the sulfidation of $CoCl_2$/GO precursor using thiourea. The

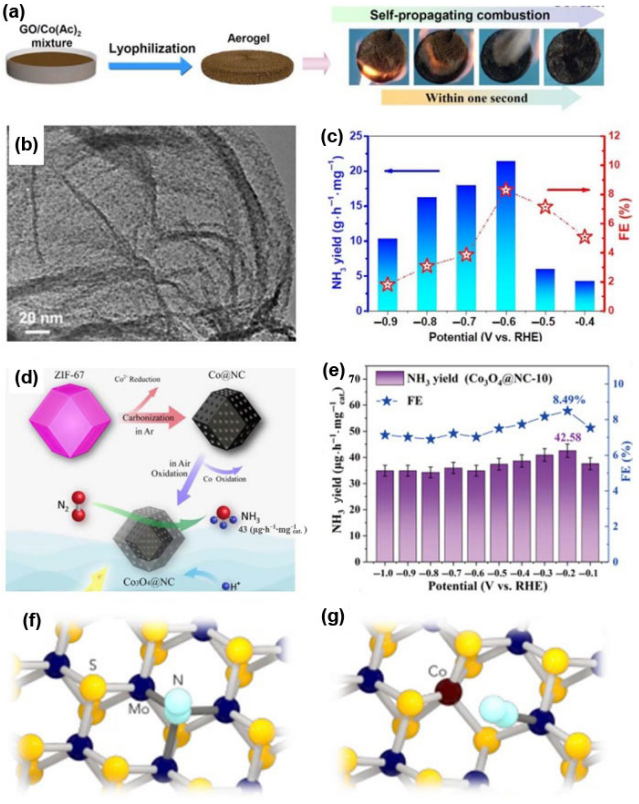

Figure 6 (a) Schematic of the synthesis process of CoO QD/rGO. (b) TEM image of CoO QD/rGO. (c) NH_3 yields and FEs of CoO QD/rGO. Reproduced with permission from Ref. [66], © The Royal Society of Chemistry 2019. (d) Schematic of the synthesis process of Co_3O_4@NCs for NRR. (e) NH_3 yields and FEs of Co_3O_4@NCs. Reproduced with permission from Ref. [95], © American Chemical Society 2019. The geometry configurations of (f) un-doped and (g) Co-doped defective MoS_{2-x} with N_2 adsorption. Reproduced with permission from Ref. [96], © American Chemical Society 2019.

Co-N/S-C bridging bond can accelerate the NRR reaction kinetics by acting as the role of electron transport channel. As a result, the CoS_2-N/S-C catalyst shows higher current density during linear sweep voltammetry test, and a high FE of 25.9% with 25 $\mu g \cdot h^{-1} \cdot mg^{-1}_{cat.}$ NH_3 yield are obtained. In our work, Co@NC thermally reduced from ZIF-67 was further vulcanized by heating with sulfur powder [41]. The structure of small-sized CoS_2 nanoparticles (average 4.4 nm) embedded in the surface of 3D nanobox (NCs) favours the exposure of more active sites for NRR. Such CoS_2@NC catalyst harvests a NH_3 yield of 17.45 $\mu g \cdot h^{-1} \cdot mg^{-1}_{cat.}$ and a FE of 4.6% at −0.15 V in 0.1 M HCl. In Luo's work [48], to avoid agglomeration and release its 2D nature, CoS nanosheets were *in situ* grown on TiO_2 nanofibrous dispersedly. To improve the conductivity, a thin carbon layer was further covered on the CoS@TiO_2 by the carbonizing of the deposited polydopamine (Figs. 7(a) and 7(b)). The obtained C@CoS@TiO_2 enables more exposed active sits and easier carrier transport during NRR process, hence attaining a FE of 28.6% and the highest NH_3 yield of 8.09 × 10^{-10} $mol \cdot s^{-1} \cdot cm^{-2}$ compared to its CoS@TiO_2 and TiO_2 counterparts.

Guo et al. expected that the active sites with unsaturated coordination on phosphide surface might be beneficial to bond the N-related intermediates and promote the NRR process [99]. They designed a CoP hollow nanocage (CoP HNC), which were derived from ZIF-67 MOF template with subsequent phosphidation of the deposited Co hydroxide via solvothermal method, as shown in Fig. 7(c). In Fig. 7(d), the TEM image shows that the hollow nanocages are covered with porous CoP nanosheets which are assembled from ultrafine (< 5 nm) nanoparticles. The abundant active sites and the beneficial mass-transferring channels contribute to the NRR performance, with a NH_3 yield of 10.78 $\mu g \cdot h^{-1} \cdot mg^{-1}_{cat.}$ and a FE of 7.36% at −0.4 V in 1.0 M KOH. An interesting phenomenon should be mentioned is that as the overpotential becoming more negative, the FE decreases but the NH_3 yield increases, which are different from the most reported catalysts where a peak performance of NH_3 production usually appeares at the optimized potential. It is easy to understand the decreased FEs by considering the

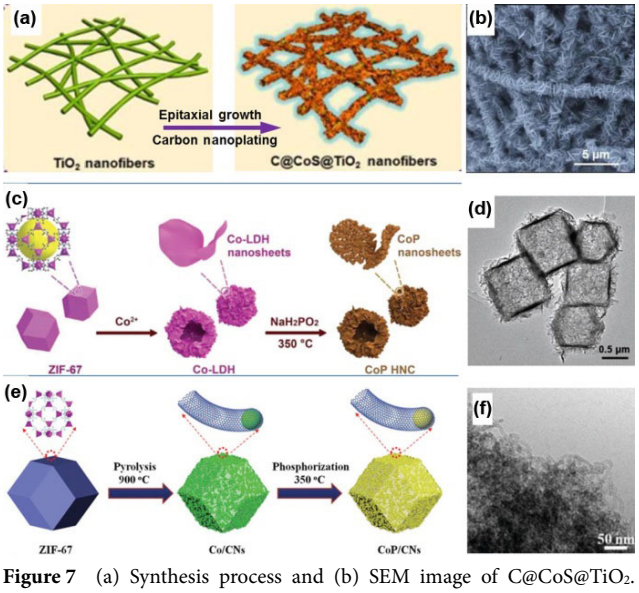

Figure 7 (a) Synthesis process and (b) SEM image of C@CoS@TiO_2. Reproduced with permission from Ref. [48], © Wiley-VCH Verlag GmbH & Co. KGaA, Weinheim 2019. (c) Synthesis process and (d) TEM image of CoP HNC. Reproduced with permission from Ref. [99], © Wiley-VCH Verlag GmbH & Co. KGaA, Weinheim 2018. (e) Synthesis process and (f) TEM image of CoP/CNS catalysts. Reproduced with permission from Ref. [100], © The Royal Society of Chemistry 2019.

gradually enhanced HER. For the increased NH_3 yield, the authors ascribe it to the high intrinsic activity of CoP HNC toward NRR. In Zhang's work [100], ZIF-67 MOF template was pyrolyzed, followed by acid washing and phosphidation (Fig. 7(e)). As observed in Fig. 7(f), the obtained catalyst shows a surface morphology covered with carbon nanotubes in which the CoP nanoparticles (CoP/CNS) were anchored. The high intrinsic activity and the exposed active sites promote the NRR performance, affording a large NH_3 yield of 48.9 $\mu g \cdot h^{-1} \cdot mg^{-1}_{cat.}$ and a FE of 8.7% at −0.4 V in 0.1 M Na_2SO_4 electrolyte. DFT calculations reveal that the unsaturated three coordinated Co sites are the effective active sites. By the distal pathway, the N_2 can be successfully activated except that the first hydrogenation step has a free energy barrier of 1.29 eV.

3.3 Ni-based electrocatalysts

NiO is also effective for NRR. In Chu's work [101], graphene was used to enhance the conductivity of NiO and avoid the aggregation of nanodots, by using the ultrafast combustion of GO/$Ni(Ac)_2$ aerogel. The resulting NiO/G catalyst (NiO nanodots on graphene) shows large electrochemical double-layer capacitance (C_{dl}), which means more exposed active sites. In 0.1 M Na_2SO_4, it exhibits a satisfied NH_3 yield of 18.6 $\mu g \cdot h^{-1} \cdot mg^{-1}_{cat.}$ and a FE of 7.8% at −0.7 V. Because of the stable catalytic activity and the strong NiO-G binding, the NiO/G also offers strong long-term durability. DFT results indicate the significant electron exchange between the adsorbed $*N_2$ and the Ni atom promotes the N_2 reduction to NH_3 by following a preferable distal pathway as confirmed of no N_2H_4 species detected in electrolyte.

It suggests that the defect-induced electron-trapping region is thermodynamically favorable for gas molecule adsorption [102]. In Li's work [103], by using Ar plasma to bombard NiO nanosheet on carbon cloth (P-NiO/CC), nanoholes around by OVs were created in the nanosheet plane (Figs. 8(a) and 8(b)). The increased OVs are confirmed by the sharp ESR signal at g = 2.004 and the larger OVs peak area deconvoluted from O 1s XPS spectra (Figs. 8(c) and 8(d)). The introduced OVs tailor the electronic structures of NiO by lowering the conduction band of NiO (Fig. 8(e)) and inducing the electron-rich configuration at the nearby Ni atom (Fig. 8(f)). As a result, the P-NiO/CC has more exposed active sites (confirmed by C_{dl} measurement), more negative N_2 adsorption energy (TPD measurement), favorable conductivity (impedance spectroscopy) and better NRR performance (reduced free energy barrier). In 0.1 M Na_2SO_4, the electrocatalyst delivers a NH_3 yield of 29.1 $\mu g \cdot h^{-1} \cdot mg^{-1}_{cat.}$ and a FE of 10.8% at −0.5 V. More interestingly, the P-NiO/CC shows even enhanced NRR activity after long-term electrolysis, which is ascribed to the new induced OVs.

Because of different electronegativities, heteroatom doping is an effective way to tailor electronic structures and modulate catalytic properties by causing charge redistribution [8]. Wang et al. [104] synthesized N-doped NiO nanosheet arrays on carbon cloth (N-NiO/CC) for NRR, by annealing the hydrothermal NiO/CC in Ar/NH_3 atmosphere (Fig. 9(a)). The N doping concentration is determined to be 2.9 at.% with Ni-O-N and N-O-N bonds as the main N-doping forms. The N-NiO/CC catalyst attains a NH_3 yield of 22.7 $\mu g \cdot h^{-1} \cdot mg^{-1}_{cat.}$ with FE of 7.3% at −0.5 V, higher than those of un-doped counterpart (Fig. 9(c)). DFT results suggest that the N-NiO has better conductivity with more occupied state electrons at the Fermi level than NiO (Fig. 9(b)), which is consistent with the smaller electron transport impedance. The project partial density of states (LDOS) ofN-NiO also presents an upshift of the d electrons band center of Ni- toward the Fermi level compared

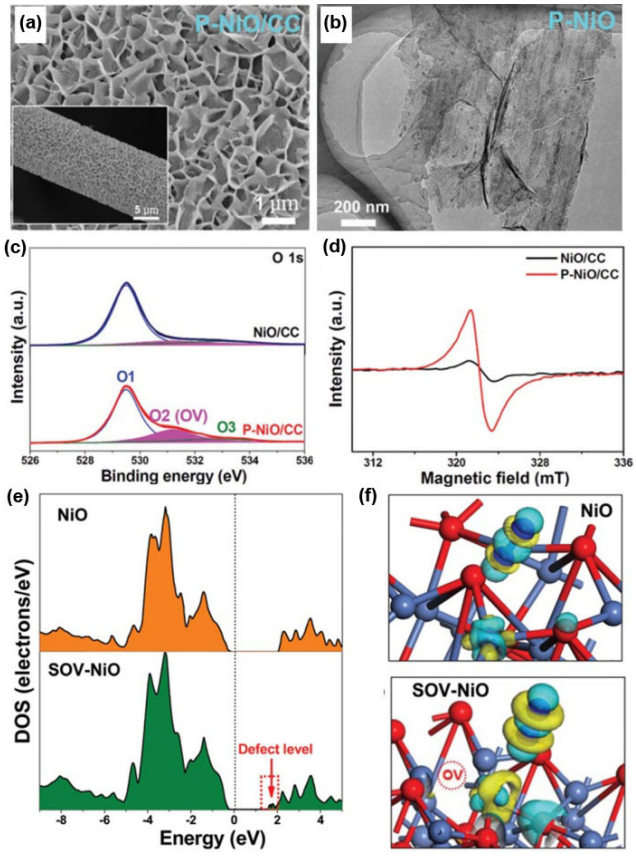

Figure 8 (a) SEM and (b) TEM images of P-NiO/CC. (c) O 1s XPS spectra and (d) ESR spectra of NiO/CC and P-NiO/CC. (e) DOS of NiO and SOV-NiO (NiO with single OV). (f) Different charge densities of absorbed $*N_2$ on NiO and SOV-NiO. Yellow and cyan denote the electron accumulation and depletion, respectively. Reproduced with permission from Ref. [103], © the Partner Organisations 2020.

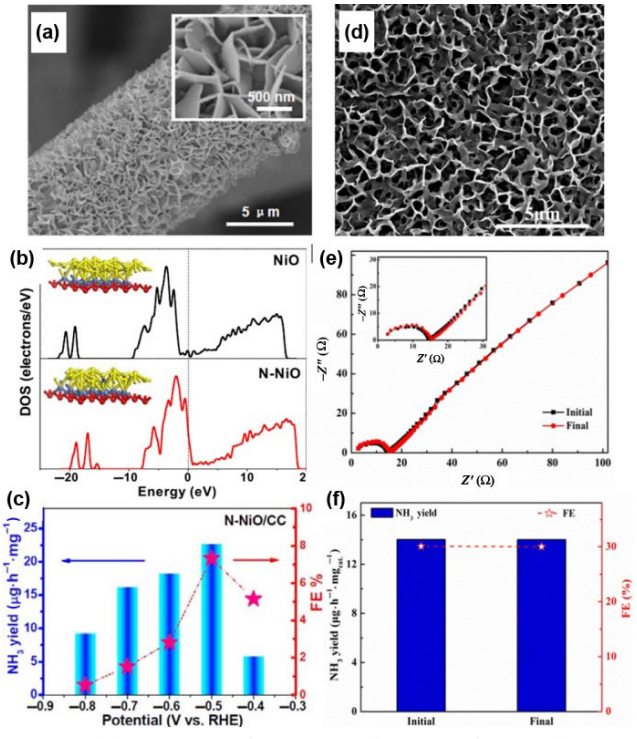

Figure 9 (a) SEM image of N-NiO/CC. (b) LDOS of NiO and N-NiO. (c) NH_3 yields and FEs of N-NiO/CC. Reproduced with permission from Ref. [104], © Wiley-VCH Verlag GmbH & Co. KGaA, Weinheim 2019. (d) SEM image of N-C@NiO/GP. (e) Nyquist plots of N-C@NiO/GP before and after long-term stability tests. (f) NH_3 yields and FEs of N-C@NiO/GP derived from 2 h electrolysis before and after long-term stability tests. Reproduced with permission from Ref. [105], © American Chemical Society 2019.

to that of NiO, implying easier electron exchange between Ni- and N_2 as well as stabilized *NNH where the formation free energy usually presents uphill feature. Interestingly, the $^{15}N_2$ label experiment indicates that $LiClO_4$ electrolyte can avoid the N atoms of N-NiO/CC to react with protons, nevertheless catalyst corrosion occurs in acid medium.

The conductivity and stability of NiO can be enhanced by coating with thin carbon layer. In Chen's work [105], the NiO nanosheets grown on graphite paper (NiO/GP) were further coated with the N-doped porous carbon by hydrothermal deposition of vitamin B8 followed by Ar annealing. The obtained N-C@NiO/GP (Fig. 9(d)) shows faster NRR kinetics (Fig. 9(e)) due to the smaller charge transfer resistance than NiO/GP, and the electrocatalyst attains a remarkable FE of 30.43% and a NH_3 yield of 14.022 $\mu g \cdot h^{-1} \cdot mg^{-1}_{cat.}$ at −0.2 V. Even though in acid (0.1 M HCl) after 20 h electrolysis, the X-ray diffraction (XRD)/SEM/XPS results confirm that the N-doped porous carbon can protect the initial NiO structure, chemical components and valent states of N-C@NiO/GP, while the NiO/GP shows destroyed morphology. As shown in Fig. 9(f), the FE and NH_3 yield of N-C@NiO/GP have negligible degeneration (30.38% and 13.977 $\mu g \cdot h^{-1} \cdot mg^{-1}_{cat.}$). This carbon-coating method would provide a promising strategy to preserve the NRR performance of metal-oxide catalyst under harsh electrochemical environments.

Bimetallic oxide is also a promising NRR catalyst with enhanced activity due to electronic redistribution and synergistic effect. Wang et al. designed a bimetallic oxide of $NiWO_4$ electrocatalyst for NRR via solvothermal method and O_2 annealing [106]. The $NiWO_4$ has porous structure composed of nanoparticles, which facilitates the transport of electrolyte and the exposure of more active sites. The coexistence of Ni and W plays a key role in boosting the NRR performance. Compared to NiO and WO_3, the $NiWO_4$ delivers the highest NH_3 yield and FE in both 0.1 M Na_2SO_4 and 0.1 M HCl, with the highest value of 40.05 $\mu g \cdot h^{-1} \cdot mg^{-1}_{cat.}$ and 19.32% in acidic medium.

3.4 Cu-based electrocatalysts

In Guo's study [107], Cu nanoparticles were anchored on rGO by hydrothermal reaction of the mixture of $Cu(Ac)_2$ and graphene powder followed by Ar/H_2 annealing (Fig. 10(a)). The uniform distribution of Cu nanoparticles can expose more active sites, while the excellent conductivity of rGO substrate enables efficient charge transfer to the active sites. As a result, the obtained Cu NPs-rGO catalyst can successfully perform N_2-to-NH_3 conversion on the top sites of Cu (111) surface, obtaining a high FE of 15.32% and a NH_3 yield of 24.58 $\mu g \cdot h^{-1} \cdot mg^{-1}_{cat.}$ at −0.4 V in 0.5 M $LiClO_4$. Dendritic Cu nanocatalyst was fabricated by us using a simple galvanic replacement method from Zn foil and $CuSO_4$ [108]. As shown in Fig. 10(b), the SEM images show that the dendritic Cu is composed of the abundant-oriented nanospikes which can not only expose abundant active sites but also amplify the local electric field near the nanospikes, which may increase the local reactant concentration and promote the reactive collision. This material shows high catalytic activity, selectivity and stability as the working electrode toward N_2 fixation, with a high FE of 15.12% and a NH_3 yield of 25.63 $\mu g \cdot h^{-1} \cdot mg^{-1}_{cat.}$ at −0.40 V in 0.1 M HCl. Lin et al. designed a Cu/PI catalyst with the Cu nanoparticles supported on polyimide (PI) for electrochemical N_2 fixation [109]. The interface interaction

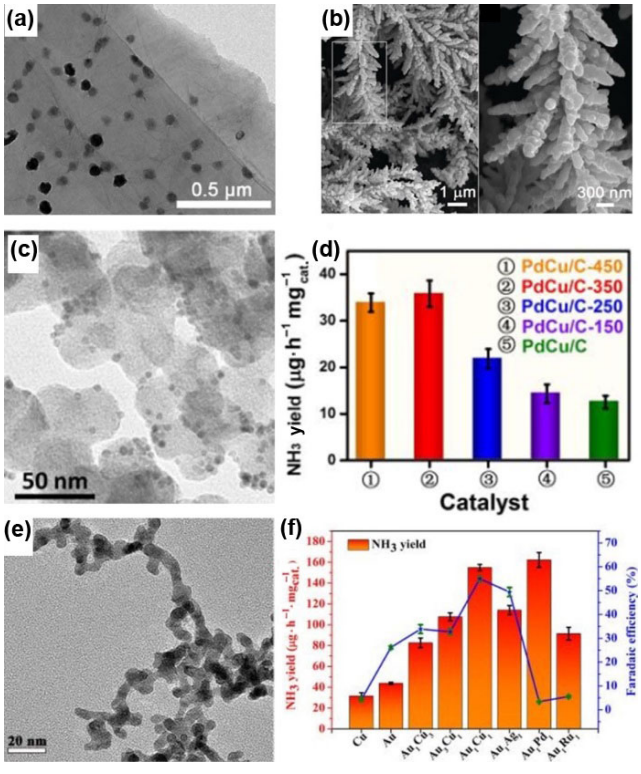

Figure 10 (a) TEM image of Cu NPs-rGO. Reproduced with permission from Ref. [107], © Elsevier 2020. (b) SEM/TEM images of dendritic Cu. Reproduced with permission from Ref. [108], © The Royal Society of Chemistry 2019. (c) TEM image of PuCu/C-350. (d) Comparison of the NH_3 yields of different PdCu catalysts at −0.1 V. Reproduced with permission from Ref. [110], © Wiley-VCH Verlag GmbH &Co. KGaA, Weinheim 2020. (e) TEM image of Au_1Cu_1. (f) Comparison of the NH_3 yields and FEs of different Au-based electrocatalysts at −0.2 V. Reproduced with permission from Ref. [111], © The Royal Society of Chemistry 2020.

tunes the electron density and causes the electron-deficient Cu nanoparticles, which suppress the HER by prohibiting the direct H^+ adsorption on active site but simultaneously enhance NRR by providing Lewis acid site to facilitate N_2 adsorption of Lewis base. The Cu/PI catalyst exhibits a NH_3 yield of 12.4 $\mu g \cdot h^{-1} \cdot mg^{-1}_{cat.}$ and a FE of 6.56% at −0.3 V in 0.1 M KOH.

Except for elemental Cu, another strategy is to alloy it with noble metals. In Tong's study, PdCu nanoalloy with ~ 5 nm spherical morphology was synthesized by a wet chemical approach [110]. To obtain well crystallinity, the PdCu nanoalloy was mixed with commercial carbon and further annealed at 350 °C. In Fig. 10(c), the obtained PdCu/C-350 remains the monodisperse spherical morphology on carbon layer but with the crystal structure transferring from face-centered cubic to body-centered cubic. DFT calculations indicate a higher electron transfer rate. Compared to PdCu/C counterpart without annealing, PdCu/C-350 shows a favorable NRR performance by the distal pathway with an energy barrier only 0.01 eV. More importantly, due to the stable crystal structure and good synergy interaction between Pd and Cu atoms, PdCu/C-350 exhibits better activity and stability. As observed in Fig. 10(d), it achieves a high NH_3 yield of 35.7 $\mu g \cdot h^{-1} \cdot mg^{-1}_{cat.}$ and a FE of 11.5% at −0.1 V in 0.5 M LiCl, which is nearly double times of improvement in NH_3 yield compared with PdCu/C. In Liu's study [111], to boost activity and avoid poor selectivity of Au-based nanocatalyst, Cu was alloyed with Au to form Au_1Cu_1 using the one-step $NaBH_4$ co-reduction method (Fig. 10(e)). It is believed that the alloy effect, which modifies the electronic structure of Au, can tune its interaction with N_2 and N_xH_y intermediates, thus boosting the NRR performance. As shown in Fig. 10(f), the Au_1Cu_1 catalyst exhibits a superior NH_3 yield of 154.91 $\mu g \cdot h^{-1} \cdot mg^{-1}_{cat.}$ and a FE of 54.96% at −0.2 V in 0.05 M H_2SO_4, outperforming its counterparts of Au_1Ag_1, Au_1Pd_1, Au_1Ru_1, Au_3Cu_1 and Au_1Cu_3.

Cao et al. [112] reported a Cu_2O-MOF with benzene-1,3,5-tricarboxylate as organic ligand. The large specific surface area favours the exposure of more active sites and greatly facilitates N_2 adsorption. The unsaturated Cu(II) sites are favorable to N_2 reduction. In 0.1 M Na_2SO_4, the electrocatalyst achieves a high NH_3 yield of 46.63 $\mu g \cdot h^{-1} \cdot mg^{-1}_{cat.}$ with FE of 2.45% at −0.75 V. CuO also presents attractive catalytic properties. Wang et al. [113] developed an active catalyst by supporting CuO nanoparticles on rGO (CuO/rGO), which delivered a high NRR performance with a NH_3 yield of 1.8×10^{-10} $mol \cdot s^{-1} \cdot cm^{-2}$ and a FE of 3.9% at −0.75 V in 0.1 M Na_2SO_4, as well as remarkable selectivity and long-term stability. DFT calculations reveal that Cu atoms are the active sites, and the NRR follows a favorable alternating pathway with the first hydrogenation as the rate-determining step.

It is worth while mentioning that Cu is also effective dopant for metal oxide toward boosted NRR activities. In our recent study, mixed-valent Cu was utilized as an dopant to modulate the VOs concentration and Ti^{3+} defect states to improve the NRR performances of TiO_2 [20]. In 0.5 M $LiClO_4$, this Cu-TiO_2 nanoparticles are capable of attaining a high FE of 21.99% with a large NH_3 yield of 21.31 $\mu g \cdot h^{-1} \cdot mg^{-1}_{cat.}$ at -0.55 V, rivaling the performances of most reported Ti-based NRR electrocatalysts. By employing hydrothermal method and H_2/Ar annealing, Zhang et al. synthesized Cu-doped CeO_2 nanorods with different doping concentrations [114]. It suggests that Cu^{2+} can replace Ce^{3+} to form multiple OVs around Cu^{2+} sites, which may act as the active sites for NRR electrocatalysis. The Cu-CeO_2 with 3.9 wt.% doping concentration delivers a NH_3 yield of 5.3×10^{-10} $mol \cdot s^{-1} \cdot cm^{-2}$ and a FE of 19.1% at −0.45 V vs. RHE in 0.1 M Na_2SO_4.

3.5 Multi-iron-based electrocatalysts

Because of the periodic electron configurations of iron group elements, multi-iron-based electrocatalysts may also have remarkable catalytic performances. In Huang's study [115], Co-doped $FePS_3$ (Co-$FePS_3$) nanosheets were synthesized by a NaCl-templated method (Fig. 11(a)). In the synthesis process, the stable and smooth surface of NaCl microcrystal in ethanol solvent provides inert planar substrate for guiding the growth of few-layered Co-$FePS_3$ nanosheets (Figs. 11(c)–11(e)). The thickness of $FePS_3$ decreases with increasing NaCl amount. DFT results indicate that Co doping enhances the conductivity of catalyst with the band gap becoming narrow, and the catalytic activities of Fe-edge sites can be significantly enhanced by the electronic orbital modulation after Co doping. The catalyst exhibits a remarkable electrocatalytic NRR performance with NH_3 yield of 90.6 $\mu g \cdot h^{-1} \cdot mg^{-1}_{cat.}$ and FE of 3.38% at −0.4 V in 0.1 M KOH. Ahmed et al. [116] designed bimetallic $CoFe_2O_4$ nanoclusters supported on rGO ($CoFe_2O_4$/rGO) for N_2 fixation. It is believed that Co doping can modulate the electronic structure of catalyst because the $4s^2d^7$ configuration of Co atom means unpaired orbitals which can influence the N_2 and N_xH_y adsorption on Fe atoms by providing beneficial electron exchange. Due to the different types of active sites (Fe, Co, rGO defects) and the more exposed active sites benefiting from the 2D nature of rGO, $CoFe_2O_4$ attains higher NH_3 yield of 4.2×10^{-11} $mol \cdot s^{-1} \cdot cm^{-2}$ and FE of 6.2% at −0.4 V in 0.1 M Na_2SO_4, compared with its monometallic counterparts [116]. In Lai's study [44], the OV-rich $NiCo_2O_4$ nanosheets were

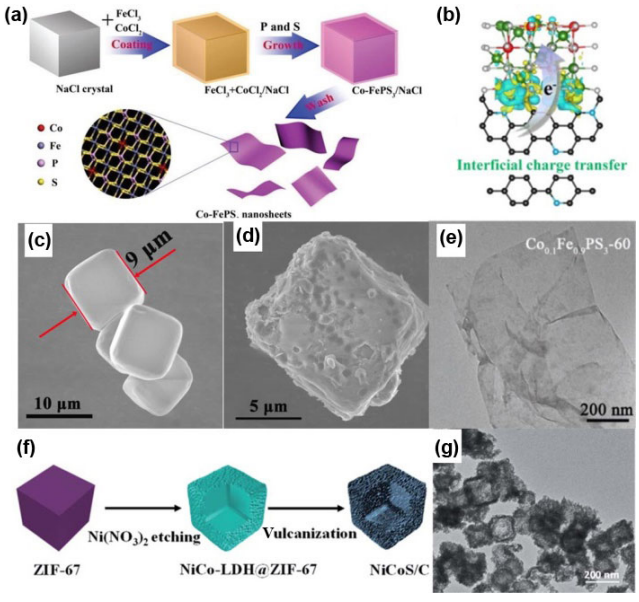

Figure 11 (a) Schematic of the synthesis process of Co-FePS$_3$ nanosheets. (b) Charge density distribution of VO-rich $NiCo_2O_4$@HNCP on the interface between VO-rich $NiCo_2O_4$ and HNCP. Reproduced with permission from Ref. [44], © The Royal Society of Chemistry 2020. SEM images of (c) NaCl template and (d) FePS$_3$-coated NaCl. (e) TEM image of Co-FePS$_3$ nanosheets. (f) Synthesis process of NiCoS/C hollow nanocages. (g) TEM image of NiCoS/C hollow nanocages. (a), (c)–(e) Reproduced with permission from Ref. [115], © Wiley-VCH Verlag GmbH &Co. KGaA, Weinheim 2019. (f) and (g) Reproduced with permission from Ref. [117], © The Royal Society of Chemistry 2020.

anchored on hollow N-carbon polyhedron (HNCP) driven from ZIF-67 template, followed by core acid etching and shell carbonization. The $NiCo_2O_4$@HNCP catalyst enables more exposed active sites of $NiCo_2O_4$. DFT calculations confirm that the OVs promote the electroactivity on the interface between VO-rich $NiCo_2O_4$ and HNCP, with abundant charge accumulating on the interface as confirmed in Fig. 11(b). The synergistic effect between $NiCo_2O_4$ and HNCP reduces the free energy barrier for NRR during the favorable enzymatic pathway. The electrocatalyst harvests a NH_3 yield of 17.8 $\mu g \cdot h^{-1} \cdot mg^{-1}_{cat.}$ and FE of 5.3% at −0.25 V in 0.1 M Na_2SO_4. In Wu's study [117], NiCoS/C hollow nanocages were fabricated by etching the ZIF-67 with $Ni(NO_3)_3$ to obtain NiCo-LDH@ZIF-67 followed vulcanization at 350 °C for 2 h (Figs. 11(f) and 11(g)). The TEM and XPS results confirm the strong chemical coupling between NiCoS and C, which not only maintains the structure stability but greatly promotes the N_2 fixation. Compared to NiCoS, NiCoS/C shows better N_2-TPD adsorption capacity. DFT results and NRR tests confirm that the coupling effect between NiCoS and C can enhance the NRR selectivity by suppressing the HER side reaction and lowering the free energy barrier at the rate-limiting step of $*N_2 \rightarrow *NNH$. Add to the more exposed active sites from the nanocage structure, the electrocatalyst achieves a high NH_3 yield of 58.5 $\mu g \cdot h^{-1} \cdot mg^{-1}_{cat.}$ at −0.2 V and a FE of 12.9% at 0 V in 0.1 M Li_2SO_4. Besides of these, bimetallic alloy is another facile route to enhance NRR performance. By employing a $NaBH_4$ reduction method in alkaline environment, Fu et al. [118] deposited Pd-Co nanoparticles onto CuO nanosheets to obtain Pd-Co/CuO electrocatalyst. The ultrathin sheet structure of CuO can support the dispersive Pd-Co nanoparticles (4–6 nm) with enlarged number of active sites. In HER tests, the amount of H_2 and FEs determined by gas chromatography show that the alloy structure enhances the NRR selectivity by suppressing HER. Compared with its monometallic counterparts, this hybrid between bimetallic alloy and nanosheet substrate greatly facilitates the NRR performance with a NH_3 yield of 10.04 $\mu g \cdot h^{-1} \cdot mg^{-1}_{cat.}$ and a FE of 2.16% in 0.1 M KOH.

4 Conclusions and outlook

In summary, we provide an overview of recent advances in designing and developing iron-group catalysts for ambient electrochemical NRR in aqueous media. As discussed above, iron-group catalysts deliver impressive NRR performances, and detailed comparisons according to the acidic, alkaline and neutral electrolyes used for electroc hemical tests are listed in Tables 1–3. Even so, deeper explorations of catalyst design and performance improvement are still necessary to simultaneously achieve large NH_3 yields and high FEs for large-scale industrial application. In the future studies, the following aspects should be considered:

(I) Rational design of efficient catalysts to promote their intrinsic activities. To overcome the sluggish NRR kinetics, an idea catalyst should adsorb and activate N_2 effectively by enabling the vibrant electronic exchange between N_2 and active site [2, 8]. Fe, Co, Ni and Cu atoms have the electronic configurations of $4s^23d^6$, $4s^23d^7$, $4s^23d^8$ and $4s^13d^{10}$, respectively, which mean empty and unoccupied orbitals of metal ions. So, iron-group catalysts exhibit great potential to drive the acceptance-donation process with the adsorbed N_2. In addition, the catalytic kinetics can be further optimized and improved by introducing vacancies, heteroatom doping, heterojunction, etc. to redistribute the charge density and tailor the electronic structure for a favorable electrocatalytic environment. The positively charged active sites can not only provide beneficial Lewis acid site to adsorb N_2 of weak Lewis base but also suppress the HER [33, 119]. The positively charged OVs can trap local metastable electrons, which are beneficial to be injected into the antibonding orbital of N≡N [35]. It is even indicated that the catalyst strain engineering can alter the electronic structures and the catalytic performances [35]. Furthermore, the catalysts design should be based on effective theory prediction and selectivity before carrying out experiments. The most exposed crystal surface, possible active sites, comparison between $*N_2$ and *H adsorptions, preferable NRR pathway should be generally predicted. A high-throughput screening is strongly recommended to quickly select out the effective catalysts, where the free energy barriers of $\Delta G_{N_2\text{-}N_2H}$ ($*N_2 \rightarrow *N_2H$) and $\Delta G_{NH_2\text{-}NH_3}$ ($*NH_2 \rightarrow *NH_3$) are set upper limit to exclude the sluggish catalysts because these two steps usually have the most positive value among the whole NRR process for most catalysts regardless of the patways [43].

(II) Structural design of catalysts to promote their apparent activities. Obviously, the number of active sites is proportional to the quantity of NRR reactions occurring on catalytic surface. Hence, except for promoting the intrinsic activity of single active site, it is equally important to expose enough active sites as many as possible. Rational arrangement of the favorable crystal surface can expose more coordination atoms and beneficial charge environment, such as by controlling the nanocrystal growth directions along nanowire, nanorod, nanosheet, etc. Moreover, single-atom or nanodot catalyst anchored on 2D substrate is a very effective way to expose active sites, maintain reaction space to relieve the site congestion, and improve the utilization efficiency of metal atoms. Of course, MOF is also very potential platform to capture N_2 molecules because of its porous structure, high specific surface area and tunable coordination atom.

Table 1 NRR performances of iron-group electrocatalysts tested in acidic electrolyes

Catalyst	Electrolyte	Potential (V vs. RHE)	NH_3 yield ($\mu g \cdot h^{-1} \cdot mg^{-1}_{cat.}$)	FE (%)	Reference
CoS_2@NC	0.1 M HCl	−0.15	17.45	4.6	[41]
porous $LaFeO_3$ nanofiber	0.1 M HCl	−0.55	18.59	8.77	[82]
Fe_3S_4 nanosheets	0.1 M HCl	−0.4	75.4	6.45	[88]
Co_3O_4@NC	0.05 M H_2SO_4	−0.2	42.58	8.5	[95]
Co-dopd MoS_{2-x}	0.01 M H_2SO_4	0.3	0.6	10	[96]
CoS_2-N/S-C	0.05 M H_2SO_4	−0.05	25	25.9	[98]
N-C@NiO/GP	0.1 M HCl	−0.2	14.022	30.43	[105]
porous $NiWO_4$	0.1 M HCl	−0.3	40.05	19.32	[106]
dendritic Cu	0.1 M HCl	−0.4	25.63	15.12	[108]
Au_1Cu_1	0.05 M H_2SO_4	−0.2	154.91	54.96	[111]

Table 2 NRR performances of iron-group electrocatalysts tested in alkaline electrolyes

Catalyst	Electrolyte	Potential (V vs. RHE)	NH_3 yield ($\mu g \cdot h^{-1} \cdot mg^{-1}_{cat.}$)	FE (%)	Reference
o-Fe_2O_3-Ar/CNT	0.1 M KOH	−0.9	0.46	6.04	[45]
γ-Fe_2O_3	0.1 M KOH	0.0	12.5	1.9	[68]
Cs/Ni-doped $LaFeO_3$	2 M KOH	2	13.46	1.99	[81]
Fe-N/C-CNTs	0.1 M KOH	−0.2	34.83	9.28	[83]
MOF(Fe)	2 M KOH	1.2	2.12×10^{-9}	1.43	[85]
FeS/Fe	0.1 M KOH	−0.3	4.13×10^{-10}	17.6	[89]
CoP HNC	1 M KOH	−0.4	10.78	7.36	[99]
Cu/PI	0.1 M KOH	−0.3	12.4	6.56	[109]
Co-$FePS_3$	0.1 M KOH	−0.4	90.6	3.38	[115]
Pd-Co/CuO	0.1 M KOH	−0.2	10.04	2.16	[118]

Table 3 NRR performances of iron-group electrocatalysts tested in neutral electrolyes

Catalyst	Electrolyte	Potential (V vs. RHE)	NH_3 yield	FE (%)	Reference
$NiCo_2O_4$@HNCP	0.1 M Na_2SO_4	−0.25	17.8 $\mu g \cdot h^{-1} \cdot mg^{-1}_{cat.}$	5.3	[44]
C@CoS@TiO_2	0.1 M Na_2SO_4	−0.55	8.09×10^{-10} $mol \cdot s^{-1} \cdot cm^{-2}$	28.6	[48]
CoO QD/rGO	0.1 M Na_2SO_4	−0.6	21.5 $\mu g \cdot h^{-1} \cdot mg^{-1}_{cat.}$	8.3	[66]
Fe_2O_3-CNT	$KHCO_3$	−2	2.2×10^{-3} $g \cdot m^{-2} \cdot h^{-1}$	—	[70]
Fe_2O_3 nanorods	0.1 M Na_2SO_4	−0.8	15.9 $\mu g \cdot h^{-1} \cdot mg^{-1}_{cat.}$	0.94	[71]
Fe_2O_3-rGO	0.5 M $LiClO_4$	−0.5	22.13 $\mu g \cdot h^{-1} \cdot mg^{-1}_{cat.}$	5.89	[72]
β-FeOOH nanorods	0.5 M $LiClO_4$	−0.75	23.32 $\mu g \cdot h^{-1} \cdot mg^{-1}_{cat.}$	6.7	[73]
β-FeO(OH,F) nanorods	0.5 M $LiClO_4$	−0.6	42.38 $\mu g \cdot h^{-1} \cdot mg^{-1}_{cat.}$	9.02	[75]
FeOOH QDs-GS	0.1 M $LiClO_4$	−0.4	27.3 $\mu g \cdot h^{-1} \cdot mg^{-1}_{cat.}$	14.6	[76]
Ti/Fe_3O_4	0.1 M Na_2SO_4	−0.4	5.6×10^{-11} $mol \cdot s^{-1} \cdot cm^{-2}$	2.6	[77]
Fe/Fe_3O_4	0.1 M PBS	−0.3	0.19 $\mu g \cdot cm^{-2} \cdot h^{-1}$	8.29	[79]
FePc/C	0.1 M Na_2SO_4	−0.3	137.95 $\mu g \cdot h^{-1} \cdot mg^{-1}_{cat.}$	10.50	[84]
ISAS-Fe/NC	0.1 M PBS	−0.4	62.9 $\mu g \cdot h^{-1} \cdot mg^{-1}_{cat.}$	18.6	[87]
FeP_2-rGO	0.5 M $LiClO_4$	−0.4	35.26 $\mu g \cdot h^{-1} \cdot mg^{-1}_{cat.}$	21.99	[90]
CoP/CNS	0.1 M Na_2SO_4	−0.4	48.9 $\mu g \cdot h^{-1} \cdot mg^{-1}_{cat.}$	8.7	[100]
NiO/G	0.1 M Na_2SO_4	−0.7	18.6 $\mu g \cdot h^{-1} \cdot mg^{-1}_{cat.}$	7.8	[101]
P-NiO/CC	0.1 M Na_2SO_4	−0.5	29.1 $\mu g \cdot h^{-1} \cdot mg^{-1}_{cat.}$	10.8	[103]
N-NiO/CC	0.1 M $LiClO_4$	−0.5	22.7 $\mu g \cdot h^{-1} \cdot mg^{-1}_{cat.}$	7.3	[104]
Cu NPs-rGO	0.5 M $LiClO_4$	−0.4	24.58 $\mu g \cdot h^{-1} \cdot mg^{-1}_{cat.}$	15.32	[107]
PdCu/C-350	0.5 M LiCl	−0.1	35.7 $\mu g \cdot h^{-1} \cdot mg^{-1}_{cat.}$	11.5	[110]
Cu_2O-MOFs	0.1 M Na_2SO_4	−0.75	46.63 $\mu g \cdot h^{-1} \cdot mg^{-1}_{cat.}$	2.45	[112]
CuO/rGO	0.1 M Na_2SO_4	−0.75	1.8×10^{-10} $mol \cdot s^{-1} \cdot cm^{-2}$	3.9	[113]
Cu-doped CeO_2	0.1 M Na_2SO_4	−0.45	5.3×10^{-10} $mol \cdot s^{-1} \cdot cm^{-2}$	19.1	[114]
$CoFe_2O_4$/rGO	0.1 M Na_2SO_4	−0.4	4.2×10^{-11} $mol \cdot s^{-1} \cdot cm^{-2}$	6.2	[116]
NiCoS/C hollow nanocages	0.1 M Li_2SO_4	−0.2	58.5 $\mu g \cdot h^{-1} \cdot mg^{-1}_{cat.}$	12.9	[117]

(III) Conductivity and stability of catalytic substrate. As discussed, apart from the hydrogenation steps concerning the participation of proton-electron pairs, the robust electron exchange between N_2 and active site plays a key role in N_2 activation to determine the NRR process. Hence, a conductive catalyst substrate is very necessary to facilitate not only the injection of electrons to the antibonding orbital of N_2 but also the following hydrogenation reactions by supplying enough reactive electrons to the active sites [2, 62, 63]. Furthermore, even though the mainly focused iron-group oxides exhibit good NRR performance, their intrinsic conductivities are poor [35]. One effective solution is to anchor the nanocatalysts on high conductive substrate. The other method must be recommended is covering a thin porous carbon layer on the catalyst surface by the carbonizing of the deposited MOF or organic polymer [48, 105]. This layer not only greatly enhances the total electrical conductivity by connecting the active sites but also keeps the structural stability of catalyst by carbon framework.

(IV) Suppressing HER. NRR is usually accompanied with the competitive HER side reaction because of the approximate standard equilibrium potentials, the possible better H^+ adsorption than N_2, and the multiple free energy barriers during hydrogenation process which may impede the active sites and then facilitate the HER. To resolve this issue, improving the catalytic selectivity to suppress HER is necessary for which it is needed to control the competitive adsorptions between N_2 and H^+ by the order sequence of N_2 priority. Besides of the DFT predictive comparison between $*N_2$ and *H adsorption energies, it is suggested to adjust the electrolyte such as by adding the organic additives to modify the H^+ adsorption environment, or using the favorable role of counterion Li^+ to increase the N_2 concentration in the Stern layer and restrict the approach of H_2O molecules to the active sites [74]. The concentrations relation between N_2 molecules and H^+ can be optimized, such as by maintaining suitable N_2 gas pressure of electrolyzer, which may promote the N_2 capture on catalyst surface meanwhile restrict the generation rate of H_2 gas [33, 37]. Further, the catalyst structures can be well exploited, such as using the nano-meso-macro structure to capture more N_2 molecules, or using N_2 gas diffusion electrode to increase the direct touching with active sites [70].

(V) Reducing the anode reaction potential and improving the utilization of anode byproducts. Even though the main goal of NRR is to obtain NH_3 at cathode, the total energy cost should be taken onto account. In aqueous solution system, oxygen evolution reaction (OER) occurs at anode, which actually needs a standard equilibrium potential as high as 1.23 V vs. RHE (far larger than the 0.092 V of NRR) [33]. It means heavy energy consumption at anode, and it is obligated to reduce the reaction potential at anode to improve the competiveness of electrocatalytic NRR with Haber-Bosch process. The oxidation potentials of many organic molecules like alcohol, hydrazine and urea are usually lower than H_2O molecules [33, 120–122], and replacing OER with anodic oxidation reaction of such molecules provides a more energy-efficient approach towards electrochemical NH_3 synthesis. Secondly, the anode materials can be optimized with highly active OER catalysts for overall electrolysis.

References

[1] Schlögl, R. Catalytic synthesis of ammonia-A "never-ending story"? *Angew. Chem., Int. Ed.* **2003**, *42*, 2004–2008.

[2] Wang, S. Y.; Ichihara, F.; Pang, H.; Chen, H.; Ye, J. H. Nitrogen fixation reaction derived from nanostructured catalytic materials. *Adv. Funct. Mater.* **2018**, *28*, 1803309.

[3] Klerke, A.; Christensen, C. H.; Nørskov, J. K.; Vegge, T. Ammonia for hydrogen storage: Challenges and opportunities. *J. Mater. Chem.* **2008**, *18*, 2304–2310.

[4] Dybkjaer, I. Ammonia production processes. In *Ammonia*, *Catalysis and Manufacture*. Nielsen, A., Ed.; Springer: Heidelberg, 1995; pp 199–308.

[5] Spatzal, T.; Aksoyoglu, M.; Zhang, L. M.; Andrade, S. L. A.; Schleicher, E.; Weber, S.; Rees, D. C.; Einsle, O. Evidence for interstitial carbon in nitrogenase FeMo cofactor. *Science* **2011**, *334*, 940.

[6] Lancaster, K. M.; Hu, Y. L.; Bergmann, U.; Ribbe, M. W.; DeBeer, S. X-ray spectroscopic observation of an interstitial carbide in NifEN-bound FeMoco precursor. *J. Am. Chem. Soc.* **2013**, *135*, 610–612.

[7] Shipman, M. A.; Symes, M. D. Recent progress towards the electrosynthesis of ammonia from sustainable resources. *Catal. Today* **2017**, *286*, 57–68.

[8] Zhu, X. J.; Mou, S. Y.; Peng, Q. L.; Liu, Q.; Luo, Y. L.; Chen, G.; Gao, S. Y.; Sun, X. P. Aqueous electrocatalytic N_2 reduction for ambient NH_3 synthesis: Recent advances in catalyst development and performance improvement. *J. Mater. Chem. A* **2020**, *8*, 1545–1556.

[9] Gao, S. Y.; Zhu, Y. Z.; Chen, Y.; Tian, M.; Yang, Y. J.; Jiang, T.; Wang, Z. L. Self-power electroreduction of N_2 into NH_3 by 3D printed triboelectric nanogenerators. *Mater. Today* **2019**, *28*, 17–24.

[10] Zhao, R. B.; Liu, C. W.; Zhang, X. X.; Zhu, X. J.; Wei, P. P.; Ji, L.; Guo, Y. B.; Gao, S. Y.; Luo, Y. L.; Wang, Z. M. et al. An ultrasmall Ru_2P nanoparticles-reduced graphene oxide hybrid: An efficient electrocatalyst for NH_3 synthesis under ambient conditions. *J. Mater. Chem. A* **2020**, *8*, 77–81.

[11] Deng, G. R.; Wang, T.; Alshehri, A. A.; Alzahrani, K. A.; Wang, Y.; Ye, H. J.; Luo, Y. L.; Sun, X. P. Improving the electrocatalytic N_2 reduction activity of Pd nanoparticles through surface modification. *J. Mater. Chem. A.* **2019**, *7*, 21674–21677.

[12] Bao, D.; Zhang, Q.; Meng, F. L.; Zhong, H. X.; Shi, M. M.; Zhang, Y.; Yan, J. M.; Jiang, Q.; Zhang, X. B. Electrochemical reduction of N_2 under ambient conditions for artificial N_2 fixation and renewable energy storage using N_2/NH_3 cycle. *Adv. Mater.* **2017**, *29*, 1604799.

[13] Liu, H. M.; Han, S. H.; Zhao, Y.; Zhu, Y. Y.; Tian, X. L.; Zeng, J. H.; Jiang, J. X.; Xia, B. Y.; Chen, Y. Surfactant-free atomically ultrathin rhodium nanosheet nanoassemblies for efficient nitrogen electroreduction. *J. Mater. Chem. A* **2018**, *6*, 3211–3217.

[14] Xiong, W.; Cheng, X.; Wang, T.; Luo, Y. S.; Feng, J.; Lu, S. Y.; Asiri, A. M.; Li, W.; Jiang, Z. J.; Sun, X. P. Co_3(hexahydroxytriphenylene)$_2$: A conductive metal-organic framework for ambient electrocatalytic N_2 reduction to NH_3. *Nano Res.* **2020**, *13*, 1008–1012.

[15] Wang, Y.; Shi, M. M.; Bao, D.; Meng, F. L.; Zhang, Q.; Zhou, Y. T.; Liu, K. H.; Zhang, Y.; Wang, J. Z.; Chen, Z. W. et al. Generating defect-rich bismuth for enhancing the rate of nitrogen electroreduction to ammonia. *Angew. Chem., Int. Ed.* **2019**, *58*, 9464–9469.

[16] Wang, J.; Liu, Y. P.; Zhang, H.; Huang, D. J.; Chu, K. Ambient electrocatalytic nitrogen reduction on a MoO_2/graphene hybrid: Experimental and DFT studies. *Catal. Sci. Technol.* **2019**, *9*, 4248–4254.

[17] Cheng, X.; Wang, J. W.; Xiong, W.; Wang, T.; Wu, T. W.; Lu, S. Y.; Chen, G.; Gao, S. Y.; Shi, X. F.; Jiang, Z. J. et al. Greatly enhanced electrocatalytic N_2 reduction over V_2O_3/C by P doping. *ChemNanoMat*, in press, DOI: 10.1002/cnma.202000110.

[18] Qin, Q.; Zhao, Y.; Schmallegger, M.; Heil, T.; Schmidt, J.; Walczak, R.; Gescheidt-Demner, G.; Jiao, H. J.; Oschatz, M. Enhanced electrocatalytic N_2 reduction via partial anion substitution in titanium oxide-carbon composites. *Angew. Chem., Int. Ed.* **2019**, *58*, 13101–13106.

[19] Xu, T.; Ma, D. W.; Li, C. B.; Liu, Q.; Lu, S. Y.; Asiri, A. M.; Yang, C.; Sun, X. P. Ambient electrochemical NH_3 synthesis from N_2 and water enabled by ZrO_2 nanoparticles. *Chem. Commun.* **2020**, *56*, 3673–3676.

[20] Wu, T. W.; Zhao, H. T.; Zhu, X. J.; Xing, Z.; Liu, Q.; Liu, T.; Gao, S. Y.; Lu, S. Y.; Chen, G.; Asiri, A. M. et al. Identifying the origin of Ti^{3+} activity toward enhanced electrocatalytic N_2 reduction over TiO_2 nanoparticles modulated by mixed-valent copper. *Adv. Mater.* **2020**, *32*, 2000299.

[21] Liu, Y. P.; Li, Y. B.; Huang, D. J.; Zhang, H.; Chu, K. ZnO quantum dots coupled with graphene toward electrocatalytic N_2 reduction: Experimental and DFT investigations. *Chem.—Eur. J.* **2019**, *25*, 11933–11939.

[22] Xia, L.; Li, B. H.; Zhang, Y.; Zhang, R.; Ji, L.; Chen, H. Y.; Cui, G. W.; Zheng, H. G.; Sun, X. P. et al. Cr_2O_3 nanoparticle-reduced graphene oxide hybrid: A highly active electrocatalyst for N_2 reduction at ambient conditions. *Inorg. Chem.* **2019**, *58*, 2257–2260.

[23] Lv, X.; Wang, F. Y.; Du, J.; Liu, Q.; Luo, Y. S.; Lu, S. Y.; Chen, G.; Gao, S. Y.; Zheng, B. Z.; Sun, X. P. Sn dendrites for electrocatalytic N_2 reduction to NH_3 under ambient conditions. *Sustain. Energy Fuels*, in press, DOI: 10.1039/D0SE00828A.

[24] Zhang, L. L.; Ding, L. X.; Chen, G. F.; Yang, X. F.; Wang, H. H. Ammonia synthesis under ambient conditions: Selective electroreduction of dinitrogen to ammonia on black phosphorus nanosheets. *Angew. Chem., Int. Ed.* **2019**, *58*, 2612–2616.

[25] Zhao, J. X.; Wang, B.; Zhou, Q.; Wang, H. B.; Li, X. H.; Chen, H. Y.; Wei, Q.; Wu, D.; Luo, Y. L.; You, J. M. et al. Efficient electrohydrogenation of N_2 to NH_3 by oxidized carbon nanotubes under ambient conditions. *Chem. Commun.* **2019**, *55*, 4997–5000.

[26] Qiu, W. B.; Xie, X. Y.; Qiu, J. D.; Fang, W. H.; Liang, R. P.; Ren, X.; Ji, X. Q.; Cui, G. W.; Asiri, A. M.; Cui, G. L. et al. High-performance artificial nitrogen fixation at ambient conditions using a metal-free electrocatalyst. *Nat. Commun.* **2018**, *9*, 3485.

[27] Zhu, X. J.; Wu, T. W.; Ji, L.; Li, C. B.; Wang, T.; Wen, S. H.; Gao, S. Y.; Shi, X. F.; Luo, Y. L.; Peng, Q. L. et al. Ambient electrohydrogenation of N_2 for NH_3 synthesis on non-metal boron phosphide nanoparticles: The critical role of P in boosting the catalytic activity. *J. Mater. Chem. A* **2019**, *7*, 16117–16121.

[28] Zhang, X. X.; Wu, T. W.; Wang, H. B.; Zhao, R. B.; Chen, H. Y.; Wang, T.; Wei, P. P.; Luo, Y. L.; Zhang, Y. N.; Sun, X. P. Boron nanosheet: An elemental two-dimensional (2D) material for ambient electrocatalytic N_2-to-NH_3 fixation in neutral media. *ACS Catal.* **2019**, *9*, 4609–4615.

[29] Zhang, Y.; Du, H. T.; Ma, Y. J.; Ji, L.; Guo, H. R.; Tian, Z. Q.; Chen, H. Y.; Huang, H.; Cui, G. W.; Asiri, A. M. et al. Hexagonal boron nitride nanosheet for effective ambient N_2 fixation to NH_3. *Nano Res.* **2019**, *12*, 919–924.

[30] Ling, C. Y.; Bai, X. W.; Ouyang, Y. X.; Du, A. J.; Wang, J. L. Single molybdenum atom anchored on N-doped carbon as a promising electrocatalyst for nitrogen reduction into ammonia at ambient conditions. *J. Phys. Chem. C* **2018**, *122*, 16842–16847.

[31] Jia, H. P.; Quadrelli, E. A. Mechanistic aspects of dinitrogen cleavage and hydrogenation to produce ammonia in catalysis and organometallic chemistry: Relevance of metal hydride bonds and dihydrogen. *Chem. Soc. Rev.* **2014**, *43*, 547–564.

[32] Jaccarino, V.; Shulman, R. G.; Stou, J. W. Nuclear magnetic resonance in paramagnetic iron group fluorides. *Phys. Rev.* **1957**, *106*, 602–603.

[33] Zhang, L. L.; Chen, G. F.; Ding, L. X.; Wang, H. H. Advanced non-metallic catalysts for electrochemical nitrogen reduction under ambient conditions. *Chem.—Eur. J.* **2019**, *25*, 12464–12485.

[34] Huang, C. S.; Li, Y. J.; Wang, N.; Xue, Y. R.; Zuo, Z. C.; Liu, H. B.; Li, Y. L. Progress in research into 2D graphdiyne-based materials. *Chem. Rev.* **2018**, *118*, 7744–7803.

[35] Wan, Y. C.; Xu, J. C.; Lv, R. T. Heterogeneous electrocatalysts design for nitrogen reduction reaction under ambient conditions. *Mater. Today* **2019**, *27*, 69–90.

[36] Li, X. F.; Li, Q. K.; Cheng, J.; Liu, L. L.; Yan, Q.; Wu, Y. C.; Zhang, X. H.; Wang, Z. Y.; Qiu, Q.; Luo, Y. Conversion of dinitrogen to ammonia by FeN_3-embedded graphene. *J. Am. Chem. Soc.* **2016**, *138*, 8706–8709.

[37] Cui, X. Y.; Tang, C.; Zhang, Q. A review of electrocatalytic reduction of dinitrogen to ammonia under ambient conditions. *Adv. Energy Mater.* **2018**, *8*, 1800369.

[38] Brown, K. A.; Harris, D. F.; Wilker, M. B.; Rasmussen, A.; Khadka, N.; Hamby, H.; Keable, S.; Dukovic, G.; Peters, J. W.; Seefeldt, L. C. et al. Light-driven dinitrogen reduction catalyzed by a CdS: Nitrogenase MoFe protein biohybrid. *Science* **2016**, *352*, 448–450.

[39] Anderson, J. S.; Cutsail III, G. E.; Rittle, J.; Connor, B. A.; Gunderson, W. A.; Zhang, L. M.; Hoffman, B. M.; Peters, J. C. Characterization of an Fe≡N–NH_2 intermediate relevant to catalytic N_2 reduction to NH_3. *J. Am. Chem. Soc.* **2015**, *137*, 7803–7809.

[40] Wang, Z.; Gong, F.; Zhang, L.; Wang, R.; Ji, L.; Liu, Q.; Luo, Y. L.; Guo, H. R.; Li, Y. H.; Gao, P. et al. Electrocatalytic hydrogenation of N_2 to NH_3 by MnO: Experimental and theoretical investigations. *Adv. Sci.* **2019**, *6*, 1801182.

[41] Wei, P. P.; Xie, H. T.; Zhu, X. J.; Zhao, R. B.; Ji, L.; Tong, X.; Luo, Y. S.; Cui, G. W.; Wang, Z. M.; Sun, X. P. CoS_2 nanoparticles-embedded N-doped carbon nanobox derived from ZIF-67 for electrocatalytic N_2-to-NH_3 fixation under ambient conditions. *ACS Sustainable Chem. Eng.* **2020**, *8*, 29–33.

[42] Zhao, P.; Lu, Z. S.; Liu, S. T. Manganese-doped CeO_2 nanocubes for catalytic combustion of chlorobenzene: An experimental and density functional theory study. *J. Nanosci. Nanotechnol.* **2018**, *18*, 3348–3355.

[43] Ling, C. Y.; Ouyang, Y. X.; Li, Q.; Bai, X. W.; Mao, X.; Du, A. J.; Wang, J. L. A general two-step strategy-based high-throughput screening of single atom catalysts for nitrogen fixation. *Small Methods* **2019**, *3*, 1800376.

[44] Lai, F. L.; Feng, J. R.; Ye, X. B.; Zong, W.; He, G. J.; Yang, C.; Wang, W.; Miao, Y. E.; Pan, B. C.; Yan, W. S. et al. Oxygen vacancy engineering in spinel-structured nanosheet wrapped hollow polyhedra for electrochemical nitrogen fixation under ambient conditions. *J. Mater. Chem. A* **2020**, *8*, 1652–1659.

[45] Cui, X. Y.; Tang, C.; Liu, X. M.; Wang, C.; Ma, W. J.; Zhang, Q. Highly selective electrochemical reduction of dinitrogen to ammonia at ambient temperature and pressure over iron oxide catalysts. *Chem.—Eur. J.* **2018**, *24*, 18494–18501.

[46] Xu, B.; Xia, L.; Zhou, F. L.; Zhao, R. B.; Chen, H. Y.; Wang, T.; Zhou, Q.; Liu, Q.; Cui, G. W.; Xiong, X. L. et al. Enhancing electrocatalytic N_2 reduction to NH_3 by CeO_2 nanorod with oxygen vacancies. *ACS Sustainable Chem. Eng.* **2019**, *7*, 2889–2893.

[47] Zhang, L.; Ji, X. Q.; Ren, X.; Ma, Y. J.; Shi, X. F.; Tian, Z. Q.; Asiri, A. M.; Chen, L.; Tang, B.; Sun, X. P. Electrochemical ammonia synthesis via nitrogen reduction reaction on a MoS_2 catalyst: Theoretical and experimental studies. *Adv. Mater.* **2018**, *30*, 1800191.

[48] Luo, Y. T.; Chen, X. X.; Yu, J. Y.; Ding, B. Carbon-nanoplated CoS@TiO_2 nanofibrous membrane: An interface-engineered heterojunction for high-efficiency electrocatalytic nitrogen reduction. *Angew. Chem., Int. Ed.* **2019**, *131*, 19079–19083.

[49] Wu, T. W.; Kong, W. H.; Zhang, Y.; Xing, Z.; Zhao, J. X.; Wang, T.; Shi, X. F.; Luo, Y. L.; Sun, X. P. Greatly enhanced electrocatalytic N_2 reduction on TiO_2 via V doping. *Small Methods* **2019**, *3*, 1900356.

[50] Li, Q. Q.; Guo, Y. L.; Tian, Y.; Liu, W. M.; Chu, K. Activating VS_2 basal planes for enhanced NRR electrocatalysis: The synergistic role of S-vacancies and B dopants. *J. Mater. Chem. A*, in press, DOI: 10.1039/D0TA05282E.

[51] Wang, Y.; Jia, K.; Pan, Q.; Xu, Y. D.; Liu, Q.; Cui, G. W.; Guo, X. D.; Sun, X. P. Boron-doped TiO_2 for efficient electrocatalytic N_2 fixation to NH_3 at ambient conditions. *ACS Sustainable Chem. Eng.* **2019**, *7*, 117–122.

[52] Li, B. Y.; Zhu, X. J.; Wang, J. W.; Xing, R. M.; Liu, Q.; Shi, X. F.; Luo, Y. L.; Liu, S. H.; Niu, X. B.; Sun, X. P. Ti^{3+} self-doped TiO_{2-x} nanowires for efficient electrocatalytic N_2 reduction to NH_3. *Chem. Commun.* **2020**, *56*, 1074–1077.

[53] Tong, W.; Huang, B. L.; Wang, P. T.; Shao, Q.; Huang, X. Q. Exposed facet-controlled N_2 electroreduction on distinct Pt_3Fe nanostructures of nanocubes, nanorods and nanowires. *Natl. Sci. Rev.*, in press, DOI: 10.1093/nsr/nwaa088.

[54] Zhang, X. X.; Liu, Q.; Shi, X. F.; Asiri, A. M.; Luo, Y. L.; Sun, X. P.; Li, T. S. TiO_2 nanoparticles-reduced graphene oxide hybrid: An efficient and durable electrocatalyst toward artificial N_2 fixation to NH_3 under ambient conditions. *J. Mater. Chem. A* **2018**, *6*, 17303–17306.

[55] Han, J. R.; Liu, Z. C.; Ma, Y. J.; Cui, G. W.; Xie, F. Y.; Wang, F. X.; Wu, Y. P.; Gao, S. Y.; Xu, Y. H.; Sun, X. P. Ambient N_2 fixation to NH_3 at ambient conditions: Using Nb_2O_5 nanofiber as a high-performance electrocatalyst. *Nano Energy* **2018**, *52*, 264–270.

[56] Zhang, Y.; Qiu, W. B.; Ma, Y. J.; Luo, Y. L.; Tian, Z. Q.; Cui, G. W.; Xie, F. Y.; Chen, L.; Li, T. S.; Sun, X. P. High-performance electrohydrogenation of N_2 to NH_3 catalyzed by multishelled hollow Cr_2O_3 microspheres under ambient conditions. *ACS Catal.* **2018**, *8*, 8540–8544.

[57] Ali, M.; Zhou, F. L.; Chen, K.; Kotzur, C.; Xiao, C. L.; Bourgeois, L.; Zhang, X. Y.; MacFarlane, D. R. Nanostructured photoelectrochemical solar cell for nitrogen reduction using plasmon-enhanced black silicon. *Nat. Commun.* **2016**, *7*, 11335.
[58] Ling, C. Y.; Niu, X. H.; Li, Q.; Du, A. J.; Wang, J. L. Metal-free single atom catalyst for N_2 fixation driven by visible light. *J. Am. Chem. Soc.* **2018**, *140*, 14161–14168.
[59] Linic, S.; Christopher, P.; Ingram, D. B. Plasmonic-metal nanostructures for efficient conversion of solar to chemical energy. *Nat. Mater.* **2011**, *10*, 911–921.
[60] Guo, C. X.; Ran, J. R.; Vasileff, A.; Qiao, S. Z. Rational design of electrocatalysts and photo(electro)catalysts for nitrogen reduction to ammonia (NH_3) under ambient conditions. *Energy Environ. Sci.* **2018**, *11*, 45–56.
[61] Zhao, J. X.; Chen, Z. F. Single Mo atom supported on defective boron nitride monolayer as an efficient electrocatalyst for nitrogen fixation: A computational study. *J. Am. Chem. Soc.* **2017**, *139*, 12480–12487.
[62] Kitano, M.; Kanbara, S.; Inoue, Y.; Kuganathan, N.; Sushko, P.; Yokoyama, T.; Hara, M.; Hosono, H. Electride support boosts nitrogen dissociation over ruthenium catalyst and shifts the bottleneck in ammonia synthesis. *Nat. Commun.* **2015**, *6*, 6731.
[63] Zhao, J. X.; Zhang, L.; Xie, X. Y.; Li, X. H.; Ma, Y. J.; Liu, Q.; Fang, W. H.; Shi, X. F.; Cui, G. L.; Sun, X. P. $Ti_3C_2T_x$ (T = F, OH) MXene nanosheets: Conductive 2D catalysts for ambient electrohydrogenation of N_2 to NH_3. *J. Mater. Chem. A* **2018**, *6*, 24031–24035.
[64] Roger, I.; Shipman, M. A.; Symes, M. D. Earth-abundant catalysts for electrochemical and photoelectrochemical water splitting. *Nat. Rev. Chem.* **2017**, *1*, 0003.
[65] Zhao, S. L.; Lu, X. Y.; Wang, L. Z.; Gale, J.; Amal, R. Carbon-based metal-free catalysts for electrocatalytic reduction of nitrogen for synthesis of ammonia at ambient conditions. *Adv. Mater.* **2019**, *31*, 1805367.
[66] Chu, K.; Liu, Y. P.; Li, Y. B.; Zhang, H.; Tian, Y. Efficient electrocatalytic N_2 reduction on CoO quantum dots. *J. Mater. Chem. A* **2019**, *7*, 4389–4394.
[67] Nguyen, M. T.; Seriani, N.; Gebauer, R. Nitrogen electrochemically reduced to ammonia with hematite: Density-functional insights. *Phys. Chem. Chem. Phys.* **2015**, *17*, 14317–14322.
[68] Kong, J. M.; Lim, A.; Yoon, C.; Jang, J. H.; Ham, H. C.; Han, J.; Nam, S.; Kim, D.; Sung, Y. E.; Choi, J. et al. Electrochemical synthesis of NH_3 at low temperature and atmospheric pressure using a γ-Fe_2O_3 catalyst. *ACS Sustainable Chem. Eng.* **2017**, *5*, 10986–10995.
[69] Liu, C. W.; Li, Q. Y.; Wu, C. Z.; Zhang, J.; Jin, Y. G.; MacFarlane, D. R.; Sun, C. H. Single-boron catalysts for nitrogen reduction reaction. *J. Am. Chem. Soc.* **2019**, *141*, 2884–2888.
[70] Chen, S. M.; Perathoner, S.; Ampelli, C.; Mebrahtu, C.; Su, D. S.; Centi, G. Electrocatalytic synthesis of ammonia at room temperature and atmospheric pressure from water and nitrogen on a carbon-nanotube-based electrocatalyst. *Angew. Chem., Int. Ed.* **2017**, *56*, 2699–2703.
[71] Xiang, X. J.; Wang, Z.; Shi, X. F.; Fan, M. K.; Sun, X. P. Ammonia synthesis from electrocatalytic N_2 reduction under ambient conditions by Fe_2O_3 nanorods. *ChemCatChem* **2018**, *10*, 4530–4535.
[72] Li, J.; Zhu, X. J.; Wang, T.; Luo, Y. L.; Sun, X. P. An Fe_2O_3 nanoparticle-reduced graphene oxide composite for ambient electrocatalytic N_2 reduction to NH_3. *Inorg. Chem. Front.* **2019**, *6*, 2682–2685.
[73] Zhu, X. J.; Liu, Z. C.; Liu, Q.; Luo, Y. L.; Shi, X. F.; Asiri, A. M.; Wu, Y. P.; Sun, X. P. Efficient and durable N_2 reduction electrocatalysis under ambient conditions: β-FeOOH nanorods as a non-noble-metal catalyst. *Chem. Commun.* **2018**, *54*, 11332–11335.
[74] Song, Y.; Johnson, D.; Peng, R.; Hensley, D. K.; Bonnesen, P. V.; Liang, L. B.; Huang, J. S.; Yang, F. C.; Zhang, F.; Qiao, R. et al. A physical catalyst for the electrolysis of nitrogen to ammonia. *Sci. Adv.*. **2018**, *4*, e1700336.
[75] Zhu, X. J.; Liu, Z. C.; Wang, H. B.; Zhao, R. B.; Chen, H. Y.; Wang, T.; Wang, F. X.; Luo, Y. L.; Wu, Y. P.; Sun, X. P. Boosting electrocatalytic N_2 reduction to NH_3 on β-FeOOH by fluorine doping. *Chem. Commun.* **2019**, *55*, 3987–3990.
[76] Zhu, X. J.; Zhao, J. X.; Ji, L.; Wu, T. W.; Wang, T.; Gao, S. Y.; Alshehri, A. A.; Alzahrani, K. A.; Luo, Y. L.; Xiang, Y. M. et al. FeOOH quantum dots decorated graphene sheet: An efficient electrocatalyst for ambient N_2 reduction. *Nano Res.* **2020**, *13*, 209–214.
[77] Liu, Q.; Zhang, X. X.; Zhang, B.; Luo, Y. L.; Cui, G. W.; Xie, F. Y.; Sun, X. P. Ambient N_2 fixation to NH_3 electrocatalyzed by a spinel Fe_3O_4 nanorod. *Nanoscale* **2018**, *10*, 14386–14389.
[78] Suryanto, B. H. R.; Kang, C. S. M.; Wang, D. B.; Xiao, C. L.; Zhou, F. L.; Azofra, L. M.; Cavallo, L.; Zhang, X. Y.; MacFarlane, D. R. Rational electrode-electrolyte design for efficient ammonia electrosynthesis under ambient conditions. *ACS Energy Lett.* **2018**, *3*, 1219–1224.
[79] Hu, L.; Khaniya, A.; Wang, J.; Chen, G.; Kaden, W. E.; Feng, X. F. Ambient electrochemical ammonia synthesis with high selectivity on Fe/Fe oxide catalyst. *ACS Catal.* **2018**, *8*, 9312–9319.
[80] Wu, T. W.; Zhu, X. J.; Xing, Z.; Mou, S. Y.; Li, C. B.; Qiao, Y. X.; Liu, Q.; Luo, Y. L.; Shi, X. F.; Zhang, Y. N. et al. Greatly improving electrochemical N_2 reduction over TiO_2 nanoparticles by iron doping. *Angew. Chem., Int. Ed.* **2019**, *58*, 18449–18453.
[81] Zhang, S.; Duan, G. Y.; Qiao, L. L.; Tang, Y.; Chen, Y. M.; Sun, Y. Z.; Wan, P. Y.; Zhang, S. J. Electrochemical ammonia synthesis from N_2 and H_2O catalyzed by doped $LaFeO_3$ perovskite under mild conditions. *Ind. Eng. Chem. Res.* **2019**, *58*, 8935–8939.
[82] Li, C. B.; Ma, D. W.; Mou, S. Y.; Luo, Y. S.; Ma, B. Y.; Lu, S. Y.; Cui, G. W.; Li, Q.; Liu, Q.; Sun, X. P. Porous $LaFeO_3$ nanofiber with oxygen vacancies as an efficient electrocatalyst for N_2 conversion to NH_3 under ambient conditions. *J. Energy Chem.* **2020**, *50*, 402–408.
[83] Wang, Y.; Cui, X. Q.; Zhao, J. X.; Jia, G. R.; Gu, L.; Zhang, Q. H.; Meng, L. K.; Shi, Z.; Zheng, L. R.; Wang, C. Y. et al. Rational design of Fe-N/C hybrid for enhanced nitrogen reduction electrocatalysis under ambient conditions in aqueous solution. *ACS Catal.* **2019**, *9*, 336–344.
[84] He, C.; Wu, Z. Y.; Zhao, L.; Ming, M.; Zhang, Y.; Yi, Y. P.; Hu, J. S. Identification of FeN_4 as an efficient active site for electrochemical N_2 reduction. *ACS Catal.* **2019**, *9*, 7311–7317.
[85] Zhao, X. R.; Yin, F. X.; Liu, N.; Li, G. R.; Fan, T. X.; Chen, B. H. Highly efficient metal-organic-framework catalysts for electrochemical synthesis of ammonia from N_2 (air) and water at low temperature and ambient pressure. *J. Mater. Sci.* **2017**, *52*, 10175–10185.
[86] Chen, Z. W.; Yan, J. M.; Jiang, Q. Single or double: Which is the altar of atomic catalysts for nitrogen reduction reaction? *Small Methods* **2019**, *3*, 1800291.
[87] Lü, F.; Zhao, S. Z.; Guo, R. J.; He, J.; Peng, X. Y.; Bao, H. H.; Fu, J. T.; Han, L. L.; Qi, G. C.; Luo, J. et al. Nitrogen-coordinated single Fe sites for efficient electrocatalytic N_2 fixation in neutral media. *Nano Energy* **2019**, *61*, 420–427.
[88] Zhao, X. H.; Lan, X.; Yu, D. K.; Fu, H.; Liu, Z. M.; Mu, T. C. Deep eutectic-solvothermal synthesis of nanostructured Fe_3S_4 for electrochemical N_2 fixation under ambient conditions. *Chem. Commun.* **2018**, *54*, 13010–13013.
[89] Xiong, W.; Guo, Z.; Zhao, S. J.; Wang, Q.; Xu, Q. Y.; Wang, X. W. Facile, cost-effective plasma synthesis of self-supportive FeS_x on Fe foam for efficient electrochemical reduction of N_2 under ambient conditions. *J. Mater. Chem. A* **2019**, *7*, 19977–19983.
[90] Zhu, X. J.; Wu, T. W.; Ji, L.; Liu, Q.; Luo, Y. L.; Cui, G. W.; Xiang, Y. M.; Zhang, Y. N.; Zheng, B. Z.; Sun, X. P. Unusual electrochemical N_2 reduction activity in an earth-abundant iron catalyst via phosphorous modulation. *Chem. Commun.* **2020**, *56*, 731–734.
[91] Liu, B.; Zhang, X. B.; Shioyama, H.; Mukai, T.; Sakai, T.; Xu, Q. Converting cobalt oxide subunits in cobalt metal-organic framework into agglomerated Co_3O_4 nanoparticles as an electrode material for lithium ion battery. *J. Power Sources* **2010**, *195*, 857–861.
[92] Liang, Y. Y.; Li, Y. G.; Wang, H. L.; Zhou, J. G.; Wang, J.; Regier, T.; Dai, H. J. Co_3O_4 nanocrystals on graphene as a synergistic catalyst for oxygen reduction reaction. *Nat. Mater.* **2011**, *10*, 780–786.
[93] Yang, J.; Yu, C.; Fan, X. M.; Liang, S. X.; Li, S. F.; Huang, H. W.; Ling, Z.; Hao, C.; Qiu, J. S. Electroactive edge site-enriched nickel-cobalt sulfide into graphene frameworks for high-performance asymmetric supercapacitors. *Energy Environ. Sci.* **2016**, *9*, 1299–1307.
[94] Wang, J. H.; Cui, W.; Liu, Q.; Xing, Z. C.; Asiri, A. M.; Sun, X. P. Recent progress in cobalt-based heterogeneous catalysts for electrochemical water splitting. *Adv. Mater.* **2016**, *28*, 215–230.
[95] Luo, S. J.; Li, X. M.; Zhang, B. H.; Luo, Z. L.; Luo, M. MOF-derived Co_3O_4@NC with core-shell structures for N_2 electrochemical reduction under ambient conditions. *ACS Appl. Mater. Interface* **2019**, *11*, 26891–26897.

[96] Zhang, J.; Tian, X. Y.; Liu, M. J.; Guo, H.; Zhou, J. D.; Fang, Q. Y.; Liu, Z.; Wu, Q.; Lou, J. Cobalt-modulated molybdenum-dinitrogen interaction in MoS_2 for catalyzing ammonia synthesis. *J. Am. Chem. Soc*. **2019**, *141*, 19269–19275.

[97] Wang, H.; Zhuo, S. F.; Liang, Y.; Han, X. L.; Zhang, B. General self-template synthesis of transition-metal oxide and chalcogenide mesoporous nanotubes with enhanced electrochemical performances. *Angew. Chem., Int. Ed*. **2016**, *55*, 9055–9059.

[98] Chen, P. Z.; Zhang, N.; Wang, S. B.; Zhou, T. P.; Tong, Y.; Ao, C. C.; Yan, W. S.; Zhang, L. D.; Chu, W. S.; Wu, C. Z. et al. Interfacial engineering of cobalt sulfide/graphene hybrids for highly efficient ammonia electrosynthesis. *Proc. Natl. Acad. Sci. USA* **2019**, *116*, 6635–6640.

[99] Guo, W. H.; Liang, Z. B.; Zhao, J. L.; Zhu, B. J.; Cai, K. T.; Zou, R. Q.; Xu, Q. Hierarchical cobalt phosphide hollow nanocages toward electrocatalytic ammonia synthesis under ambient pressure and room temperature. *Small Methods* **2018**, *2*, 1800204.

[100] Zhang, S. B.; Gong, W. B.; Lv, Y.; Wang, H. J.; Han, M. M.; Wang, G. Z.; Shi, T. F.; Zhang, H. M. A pyrolysis-phosphorization approach to fabricate carbon nanotubes with embedded CoP nanoparticles for ambient electrosynthesis of ammonia. *Chem. Commun*. **2019**, *55*, 12376–12379.

[101] Chu, K.; Liu, Y. P.; Wang, J.; Zhang, H. NiO nanodots on graphene for efficient electrochemical N_2 reduction to NH_3. *ACS Appl. Energy Mater*. **2019**, *2*, 2288–2295.

[102] Zhang, N.; Jalil, A.; Wu, D. X.; Chen, S. M.; Liu, Y. F.; Gao, C.; Ye, W.; Qi, Z. M.; Ju, H. X.; Wang, C. M. et al. Refining defect states in $W_{18}O_{49}$ by Mo doping: A strategy for tuning N_2 activation towards solar-driven nitrogen fixation. *J. Am. Chem. Soc*. **2018**, *140*, 9434–9443.

[103] Li, Y. B.; Liu, Y. P.; Wang, J.; Guo, Y. L.; Chu, K. Plasma-engineered NiO nanosheets with enriched oxygen vacancies for enhanced electrocatalytic nitrogen fixation. *Inorg. Chem. Front*. **2020**, *7*, 455–463.

[104] Wang, X. H.; Wang, J.; Li, Y. B.; Chu, K. Nitrogen-doped NiO nanosheet array for boosted electrocatalytic N_2 reduction. *ChemCatChem* **2019**, *11*, 4529–4536.

[105] Chen, Y. J.; Wu, B.; Sun, B. L.; Wang, N.; Hu, W. C.; Komarneni, S. N-Doped porous carbon self-generated on nickel oxide nanosheets for electrocatalytic N_2 fixation with a faradaic efficiency beyond 30%. *ACS Sustainable Chem. Eng*. **2019**, *7*, 18874–18883.

[106] Wang, J.; Jang, H.; Li, G. K.; Kim, M. G.; Wu, Z. X.; Liu, X. E.; Cho, J. Efficient electrocatalytic conversion of N_2 to NH_3 on $NiWO_4$ under ambient conditions. *Nanoscale* **2020**, *12*, 1478–1483.

[107] Guo, X. X.; Yi, W. C.; Qu, F. L.; Lu, L. M. New insights into mechanisms on electrochemical N_2 reduction reaction driven by efficient zero-valence Cu nanoparticles. *J. Power Sources* **2020**, *448*, 227417.

[108] Li, C. B.; Mou, S. Y.; Zhu, X. J.; Wang, F. Y.; Wang, Y. T.; Qiao, Y. X.; Shi, X. F.; Luo, Y. L.; Zheng, B. Z.; Li, Q. et al. Dendritic Cu: A high-efficiency electrocatalyst for N_2 fixation to NH_3 under ambient conditions. *Chem. Commun*. **2019**, *55*, 14474–14477.

[109] Lin, Y. X.; Zhang, S. N.; Xue, Z. H.; Zhang, J. J.; Su, H.; Zhao, T. J.; Zhai, G. Y.; Li, X. H.; Antonietti, M.; Chen, J. S. Boosting selective nitrogen reduction to ammonia on electron-deficient copper nanoparticles. *Nat. Commun*. **2019**, *10*, 4380.

[110] Tong, W.; Huang, B. L.; Wang, P. T.; Li, L. G.; Shao, Q.; Huang, X. Q. Crystal-phase-engineered PdCu electrocatalyst for enhanced ammonia synthesis. *Angew. Chem., Int. Ed*. **2020**, *59*, 2649–2653.

[111] Liu, Y. Q.; Huang, L.; Zhu, X. Y.; Fang, Y. X.; Dong, S. J. Coupling Cu with Au for enhanced electrocatalytic activity of nitrogen reduction reaction. *Nanoscale* **2020**, *12*, 1811–1816.

[112] Cao, Y. M.; Li, P. P.; Wu, T. T.; Liu, M. L.; Zhang, Y. Y. Electrocatalysis of N_2 to NH_3 by HKUST-1 with high NH_3 yield. *Chem.—Asian J*. **2020**, *15*, 1272–1276.

[113] Wang, F.; Liu, Y. P.; Zhang, H.; Chu, K. CuO/graphene nanocomposite for nitrogen reduction reaction. *ChemCatChem* **2019**, *11*, 1441–1447.

[114] Zhang, S. B.; Zhao, C. J.; Liu, Y. Y.; Li, W. Y.; Wang, J. L.; Wang, G. Z.; Zhang, Y. X.; Zhang, H. M.; Zhao, H. J. Cu doping in CeO_2 to form multiple oxygen vacancies for dramatically enhanced ambient N_2 reduction performance. *Chem. Commun*. **2019**, *55*, 2952–2955.

[115] Huang, H.; Li, F. M.; Xue, Q.; Zhang, Y.; Yin, S. W.; Chen, Y. Salt-templated construction of ultrathin cobalt doped iron thiophosphite nanosheets toward electrochemical ammonia synthesis. *Small* **2019**, *15*, 1903500.

[116] Ahmed, M. I.; Chen, S.; Ren, W. H.; Chen, X. J.; Zhao, C. Synergistic bimetallic $CoFe_2O_4$ clusters supported on graphene for ambient electrocatalytic reduction of nitrogen to ammonia. *Chem. Commun*. **2019**, *55*, 12184–12187.

[117] Wu, X. K.; Wang, Z. C.; Han, Y.; Zhang, D.; Wang, M. H.; Li, H. D.; Zhao, H.; Pan, Y.; Lai, J. P.; Wang, L. Chemically coupled NiCoS/C nanocages as efficient electrocatalysts for nitrogen reduction reactions. *J. Mater. Chem. A* **2020**, *8*, 543–547.

[118] Fu, W. Z.; Cao, Y. D.; Feng, Q. Y.; Smith, W. R.; Dong, P.; Ye, M. X.; Shen, J. F. Pd-Co nanoalloys nested on CuO nanosheets for efficient electrocatalytic N_2 reduction and room-temperature Suzuki-Miyaura coupling reaction. *Nanoscale* **2019**, *11*, 1379–1385.

[119] Yuan, L. P.; Wu, Z. Y.; Jiang, W. J.; Tang, T.; Niu, S.; Hu, J. S. Phosphorus-doping activates carbon nanotubes for efficient electroreduction of nitrogen to ammonia. *Nano Res*. **2020**, *13*, 1376–1382.

[120] Tang, C.; Zhang, R.; Lu, W. B.; Wang, Z.; Liu, D. N.; Hao, S.; Du, G.; Asiri, A. M.; Sun, X. P. Energy-saving electrolytic hydrogen generation: Ni_2P nanoarray as a high-performance non-noble-metal electrocatalyst. *Angew. Chem., Int. Ed*. **2017**, *56*, 842–846.

[121] Wang, J. M.; Ma, X.; Liu, T. T.; Liu, D. N.; Hao, S.; Du, G.; Kong, R. M.; Asiri, A. M.; Sun, X. P. NiS_2 nanosheet array: A high-active bifunctional electrocatalyst for hydrazine oxidation and water reduction toward energy-efficient hydrogen production. *Mater. Today Energy* **2017**, *3*, 9–14.

[122] Liu, D. N.; Liu, T. T.; Zhang, L. X.; Qu, F. L.; Du, G.; Asiri, A. M.; Sun, X. P. High-performance urea electrolysis towards less energy-intensive electrochemical hydrogen production using a bifunctional catalyst electrode. *J. Mater. Chem. A* **2017**, *5*, 3208–3213.